DESIGN AND ANALYSIS OF A ROBOTIC TENSEGRITY DOLPHIN

A Thesis

by

CHRISTOPHER L. PLANTZ

Submitted to the Graduate and Professional School of
Texas A&M University
in partial fulfillment of the requirements for the degree of

MASTER OF SCIENCE

Chair of Committee,	Robert Skelton
Co-Chair of Committee,	Hamn C. Chen
Committee Member,	Iman Borazjani
Head of Department,	Sharath Girimaji

August 2021

Major Subject: Ocean Engineering

Copyright 2021 Christopher L. Plantz.

ABSTRACT

This thesis offers an overview of tensegrity systems and the historical and novel research and development of swimming robotics. A robotic dolphin (with two tail designs) was designed and manufactured using a tensegrity theory approach and experimentally analyzed for its biomimetic capabilities. The simple tail structure (i.e. one with less vertebrae) was found to be more efficient at producing thrust with the given low thrust servomotor (35kg-cm). The observed swimming performance was characteristic of Strouhal numbers in the range of $0.57 < St < 0.84$. The relationship between forward speed and tail beat frequency was found to be linear in frequencies from $0.83 < f < 2.38$ Hz, in which tail beat amplitude decreased significantly with increasing frequency.

The flexing tail structure was modeled as a morphing airfoil through the control of string pretension and length change, as a first step towards implementation of information architecture in future studies. In addition, CFD was used to simulate turbulence, boundary layer characteristics, and coefficients of drag. Two turbulence models, SST k-omega and k-epsilon, were compared and it was found that the k-epsilon method may underpredict frictional drag by roughly 7% at Re = 3.1e6. Laminar-turbulent flow transitions were calculated near Re = 6e5 – 7e5 for the gliding dolphin at straight body position. With increasing Reynolds number, delaying of flow separation along the body surface, as well as a narrowing of the wake was found. Preliminary data suggests narrowing of the wake through modifying the dolphin body with a bulbous melon.

DEDICATION

I dedicate this research to my grandparents, Mr. Andrew Plantz, Mrs. Shirley Plantz, Mr. Larry Sheppard, and Mrs. Sylvia Sheppard, who may not be here to read my thesis, but I know are watching over me as guardian angels.

ACKNOWLEDGEMENTS

I would like to thank Dr. Skelton for guiding me through the complexity of design and control of tensegrity systems, and for introducing me to a field of engineering I never knew I would study. Dr. Skelton always has a great story to tell and has given me great inspiration to explore all aspects of science and engineering.

I would also like to thank Dr. Chen for his wonderful skills in teaching the fundamentals of computational fluid dynamics. Dr. Chen's homework assignments and exams were very crucial in my understanding of ocean engineering. His many contributions to academia, research and development are outstanding and have motivated me to always strive for success.

Dr. Borazjani offered me extensive knowledge about swimming kinematics that have shaped my research and knowledge of swimming kinematics. Dr. Borazjani's PhD student, Amir Akbarzadeh, walked me through elongated body theory and made sure I fully understood all the equations and derivations. For that, I would like to thank both Dr. Borazjani and Amir Akbarzadeh for their amazing help.

I would also like to thank Dr. Muhao Chen for being a mentor and a friend. Muhao helped me through all my thesis, always offering advice and knowledge. He is a great friend who I enjoy discussing not only engineering, but also life in general with. His wisdom has changed my viewpoint of the world for the better.

To my mother Lynn, father Jeffrey, brothers Mark and John, and my love, Victoria, I thank you for providing me with mental support throughout my studies and the Covid-19 pandemic. These five people will forever hold a special place in my heart.

CONTRIBUTORS AND FUNDING SOURCES

Contributors

This work was supervised by Dr. Robert Skelton of the Department of Aerospace Engineering, Dr. Hamn C. Chen of the Department of Ocean Engineering, and Dr. Iman Borazjani of the Department of Mechanical Engineering.

The derivations in Chapter 1 were conducted in part by Muhao Chen, Jiacheng Liu, Raman Goyal, and Dr. Robert Skelton of the Department of Aerospace Engineering and were published in 2019-2020.

All other work conducted for the thesis, unless cited, was completed by the student independently

Funding Sources

Funding for the purchase of all necessary products to conduct this thesis was provided by the Department of Aerospace Engineering and personal funds.

TABLE OF CONTENTS

Page

LIST OF FIGURES

Page

Page

LIST OF TABLES

Page

CHAPTER I

INTRODUCTION

1.1 Tensegrity Theory

The term tensegrity was first introduced within an architectural patent of Buckminster Fuller in 1959, describing structures that achieve integrity through tension [1] [2]. A decade earlier, the artist Kenneth Snelson invented tensegrity through building structures without terming or patenting the design [2]. One of Snelson's works, "X-piece" (1948) is a structure composed of two rigid "X" bodies suspended in the air and strung together by cables [2]. The cables use tensile forces to produce compressive forces on each rigid body and ultimately hold the structure in a stable system without the rigid bodies coming into contact.

In the textbook "Tensegrity Structures" written by Robert Skelton and Maurício de Oliveira, tensegrity is given an engineering definition: a set of rigid bodies that, with no external forces, can be held in a stable equilibrium configuration using internal tensile members such as strings or cables [2]. As a fundamental building block of more complex structures, Skelton and de Oliveira present the tensegrity prism, consisting of internal bars held in compression by external strings as seen in figure 1.1 [5].

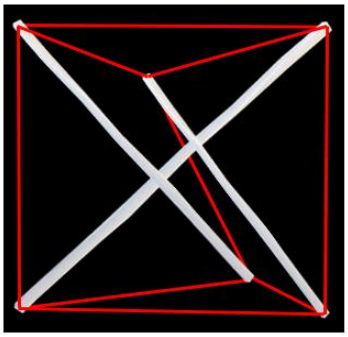

Figure 1.1. A 3D tensegrity prism consisting of 3 bars (white) and 9 strings (red).

These prisms can be configured to allow for rotational twisting either in the clockwise or counterclockwise direction, and when stacked or arranged with other prisms, can create twistable columns, antennas, satellites, wings, and many more as discussed in section 1.2.

The prism in figure 1.1 is denoted as a class 1 tensegrity structure because the rigid bars are not directly in contact with each other [2]. A class 2 tensegrity structure would mean there are two bars in contact, or more generally, a class k tensegrity structure would consist of k bars in contact. For two rigid bodies to be connected, there must be a joint (i.e. ball joint) at the connection node, or otherwise the two bars would effectively act as a single member.

1.2 Tensegrity Applications

Most importantly, tensegrity structures can be designed to have multiple configurations, or equilibria, in which they switch between by altering tension within each string. Skelton and de Oliveira note that tensegrity structures can make these changes without drastically altering their mechanical properties [2]. For example, a structure can switch from one equilibrium to another of different geometry while retaining the same structural stiffness [2].

As did the invention of the truss, tensegrity allows for minimal mass design and goes even further to rule out the effects of moments by preventing each member from experiencing both compression and tension [2]. In fact, tensegrities are a specific type of truss, and throughout a wide range of engineering applications, it is possible to build structures of high strength and low mass.

1.2.1 Aerospace Tensegrities

Aerospace applications include the design and modeling of bendable airfoils, dampening planetary landers and adjustable satellite solar arrays. Chen et al. (2020) outline a non-linear

control and numerical study of morphing tensegrity airfoils [3]. A physical prototype of a bending wing can be seen in figure 1.2.

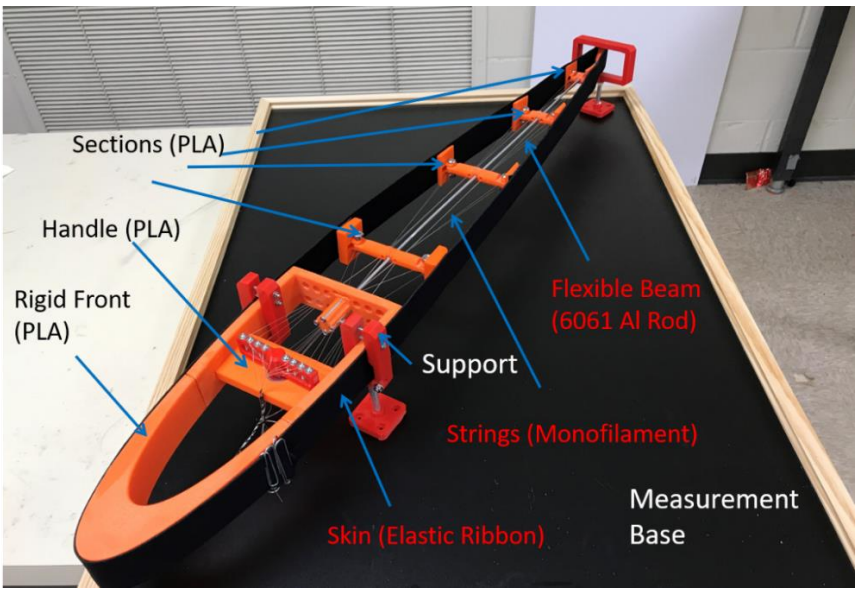

Figure 1.2. Tensegrity airfoil by Muhao Chen – Texas A&M – Dept. of Aerospace Eng.

As the monofilament fibers seen travelling down the middle of the airfoil are tensed, the flexible beam, seen down the camber line of the foil, and the elastic skin along the surface of the foil will flex to a desired, low angle of attack.

1.2.2 Architectural Tensegrities

Architectural design can employ tensegrity to allow buildings and homes to adjust shape and geometry in response to earthquakes, high winds, or to capture and block solar energy for an eco-friendly approach to heating, cooling, and lighting [2]. As a model for a skyscraper, tensegrity prisms, as seen in figure 1.3, can be stacked on top of each other to create a column as discussed in Skelton and de Oliveira [2].

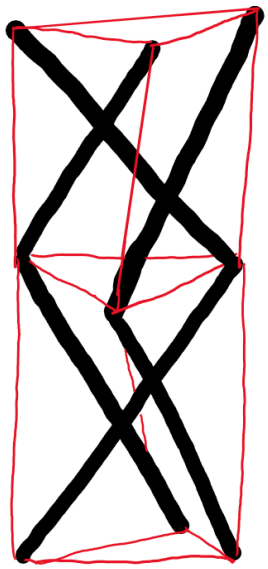

Figure 1.3. Tensegrity tower with twistable shape control.

Figure 1.3 is a crude estimation of a tower composed of two stacked tensegrity prisms. Depending on how each prism is configured respectively to each other, the rotational direction of twist will be different, and thus by stacking these prisms in various ways, a variable flexing structure can be modeled.

1.2.3 Marine Tensegrities

In ocean engineering, as in this paper, tensegrity theory can be used to design deployable buoy stations, robotic arms for ocean floor sampling, or AUVs for marine surveying [2]. Skelton and de Oliveira present the first wave-powered vehicle as a station keeping buoy consisting of a submersible tensegrity structure and thruster [2]. The benefits of this design are that the buoy is deployable and so does not take up much space during transportation, and that it has a longer lifespan than conventional battery-powered buoys [2]. Station-keeping capabilities are important throughout all of ocean engineering, be it for buoys, offshore structures, or submersible vehicles.

To improve the speed and efficiency of underwater vehicles, this paper looks to the biological nature of fish for motivation to replace conventional propeller systems.

1.2.4 Tensegrity in Nature

Tensegrities seen in biology and nature are arguably the most complex applications of tensegrity architecture. Long before man-made theory and engineering design, the use of strings and rigid bars has built several examples of tensegrity structures, such as spider webs, appendicular tendons, red blood cells, and DNA [2] [4].

Much like the prism in figure 1.1, Liedl et al. (2010) have presented self-assembled DNA tensegrities composed of DNA double helices (rigid bars) and single stranded DNA (string/springs) [4]. Here, it is seen that even on the nanoscale, the basic building block of animal and man can be used to generate tensegrity structures that model closely the cellular systems employed in living organisms [4]. Liedl et al. (2010) even go on to calculate string lengths and tensile forces, which play a crucial role in the design, control, and information architecture of tensegrity systems as discussed in section 1.11.

Another reason biological tensegrities are so complex is because of the neural networks responsible for the entrainment of body movements, such as that of a swimming fish or flying bird. These neural networks are called Central Pattern Generators (CPGs), and they allow animals to move their muscles for efficient and effective locomotion. Artifical CPGs have promise for implimentation into biomimetic tesnegrity robots, which this thesis hopes to inspire in future works.

1.3 Rotational Dynamics

Before building a tensegrity structure, we begin by defining dynamics of the bar components that make up these configurations. For a rigid bar in 3D space the dynamics can be visualized in figure 1.4.

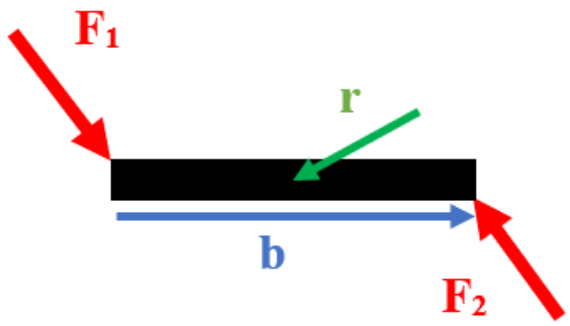

Figure 1.4. Description of a tensegrity bar member with external forces.

The above black bar is defined along the body-fixed vector b, with length l = $\|b\|$ and center of mass located by the vector r. F_1 and F_2 represent the external forces, such as tension in strings attached to the end of each bar. Following the derivation in Goyal and Skelton (2019), the angular velocity of a tensegrity bar is calculated as

$$\omega = \frac{b \times \dot{b}}{\|b\|^2} = \frac{b \times \dot{b}}{l^2}. \tag{1}$$

Angular momentum (h) of the bar is then given by the product of angular velocity and inertia of a solid cylinder:

$$h = \left(\frac{ml^2}{12} + \frac{mr^2}{4}\right)\left(\frac{b \times \dot{b}}{l^2}\right) = Jb \times \dot{b}\,, \tag{2}$$

where m is the mass of the cylindrical bar. The inertia of a solid bar is given in the first term of the above equation [5]. The torque experienced by the bar is calculated as the sum of forces multiplied by the moment arm with respect to the center of mass ($\pm$b/2). Torque is also equal to the time rate of change of angular momentum [5]:

$$\tau = Jb \times \ddot{b}. \tag{3}$$

Since it is desired for each bar member to act as rigid members, they must have constant length (l) such that the expression $b^T b = l^2$ holds true for each bar [5]. Thus, the fully defined rotational dynamics for constant length bar members in matrix form is

$$\begin{bmatrix} \tilde{b} \\ b^T \end{bmatrix} \ddot{b} = \begin{bmatrix} \frac{1}{2J}\tilde{b}(f_2 - f_1) \\ -\dot{b}^T \dot{b} \end{bmatrix}, \tag{4}$$

where $\tilde{b}$ is the skew symmetric matrix of bar vector b.

1.4 Translational Dynamics

The dynamics of a tensegrity member is not purely rotational, and thus here we define the translational dynamics of a rigid bar member. Using the same bar member illustrated in figure 1.4, the sum of forces with respect to the center of mass is $\sum F = f_1 + f_2$. From Newton's second law of motion, the acceleration of the center of mass of each bar is found by

$$m\ddot{r} = f_1 + f_2 \tag{5}$$

1.5 Matrix Form of Dynamics

For a tensegrity system of several bar members, the dynamic problem can be easily solved in matrix form [5]. The following variables and matrices are shown in table 1.1.

Table 1.1. Matrices and variables used to define dynamic tensegrities.

Matrix of nodes	N
Matrix of strings	S
Matrix of bar vectors	B
Matrix of bar mass centers	R
String connectivity matrix	C_s
Bar connectivity matrix	C_b
Bar mass center matrix	C_r
Force Matrix	F
External Forces	W
Tension	T
Internal Forces	TC_s
String Density	γ

The matrix $N = [N_1\ N_2]$ is the three-dimensional locations of each node, where a node is defined by the two endpoints of a bar. N_1 is by convention termed the base node such that the center of mass matrix is $R = N_1 + B/2 = NC_r^T$ [5]. Thus, a tensegrity structure consisting of β bar members will have 2β nodes such that $B = [b_1\ b_2\ \dots\ b_\beta]$, $N_1 = [n_1\ n_2\ \dots\ n_\beta]$, and $N_2 = [n_{1+\beta}\ n_{2+\beta}\ \dots\ n_{2\beta}]$ [5]. The matrices S and B represent three-dimensional direction vectors of each string and bar such that the strings and bars are formed in physical space by expressing $S = NC_s^T$ and $B = NC_b^T$, generating a tensegrity model that consists of bar-to-bar and bar-to-string connections [5].

Goyal and Skelton (2019) define a force matrix F to describe the forces acting upon each endpoint of the bar members such that $f_2 - f_1 = FC_b^T$. By using the previously defined matrices F, B and S, and defining the variable $\hat{\lambda}$ as the force density in each bar, the combined rotational and translational dynamics in matrix form are written as

$$\ddot{N}\left(C_b^T \hat{J} C_b + C_r^T \hat{m}_b C_r\right) - N\left(C_b^T \hat{\lambda} C_b\right) = F. \tag{6}$$

where $\hat{J}$ is the diagonal matrix of inertia (J) with diagonals $J_1 \ldots J_\beta$, and $\hat{l}$ is the diagonal matric of length (l) with diagonals $l_1 \ldots l_\beta$ [5]. The general outline of tensegrity dynamics offered here can be found in more detail in Goyal and Skelton (2019) [5].

1.6 Fully Defined Force Matrix

The force matrix F is composed of external forces W (such as hydrodynamics forces, winds, or other environmental forces) and internal forces TC_s where tension T is defined in terms of string force density γ, such that $T = S\hat{\gamma} = NC_s^T \hat{\gamma} C_s$ [5]. It follows that the fully defined force experienced by a tensegrity structure is

$$\ddot{N}\left(C_b^T \hat{J} C_b + C_r^T \hat{m}_b C_r\right) + N\left(C_s^T \hat{\gamma} C_s - C_b^T \hat{\lambda} C_b\right) = W. \tag{7}$$

For a more compact matrix form, the matrices M, K, and W are defined, such that equation three can expressed as

$$\ddot{N}M + NK = W, \tag{8}$$

where $M = C_b^T \hat{J} C_b + C_r^T \hat{m}_b C_r$, and $K = C_s^T \hat{\gamma} C_s - C_b^T \hat{\lambda} C_b$ [5].

1.7 Massive Strings

In the previous dynamics, the strings are considered to have zero mass. In physical tensegrity models, however, the strings will have mass and thus the dynamics must be redefined. Goyal and Skelton (2019) achieve this by dividing the strings into smaller segments, each attached via point masses. In figure 1.5 below, the connecting point masses can be visualized.

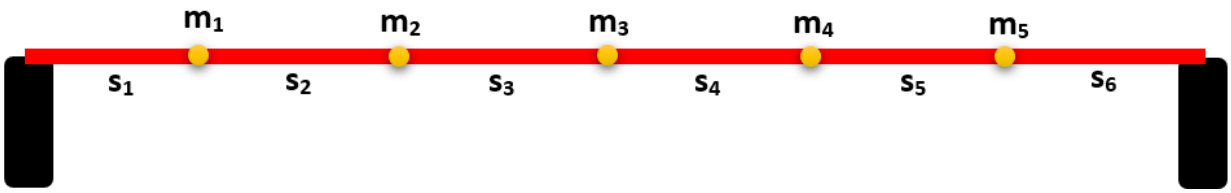

Figure 1.5. A string (red) within a tensegrity system consisting of two bars (black).

As can be seen in the figure 1.5, each string within any tensegrity system can be subdivided into N segments and N-1 point masses, such that the total mass of the string is the summation of each point mass ($M = \sum_{n=1}^{n=N-1} m_n$).

With the newly defined massive strings, the matrices N, R, S and F are divided into two components to represent bars (b) and strings (s), such that

$$N_b = NC_{nb}^T, \tag{9}$$

$$N_s = NC_{ns}^T, \tag{10}$$

$$R_b = N_b C_r^T \tag{11}$$

$$R_s = N_s, \tag{12}$$

$$S = NC_s^T = [N_b \quad N_s]\begin{bmatrix} C_{sb}^T \\ C_{ss}^T \end{bmatrix}, \tag{13}$$

and

$$F = [F_b \quad F_s] = W - NC_s^T \hat{\gamma} C_s \,, \tag{14}$$

where C_{sb} and C_{ss} are string-bar and string-string connections. Now, the dynamics of each bar can be expressed as

$$\ddot{B}\hat{J} = \frac{1}{2} F_b C_b^T + B\hat{\lambda}, \tag{15}$$

$$\hat{\lambda} = -\hat{J}\hat{l}^{-2}\left\lfloor \dot{B}^T \dot{B} \right\rfloor - \frac{1}{2}\hat{l}^{-2}\lfloor B^T F_b C_b^T \rfloor, \tag{16}$$

and

$$\ddot{R}_b \hat{m}_b = 2F_b C_r^T. \tag{17}$$

For simplicity, the detailed procedure outlined by Goyal and Skelton (2019) is omitted from this thesis. However, in summary, the above three equations are rewritten in matrix form, and with the definition of the orthogonal matrix $[0.5C_b^T \quad 2C_r^T]^{-1} = [C_b^T \quad C_r^T]^T$, the complete system dynamics with massive strings is given by

$$\ddot{N}[C_{nb}^T C_b^T \hat{J} C_b + C_{nb}^T C_r^T \hat{m}_b C_r \quad C_{ns}^T \hat{m}_s] + N[C_s^T \hat{\gamma} C_{sb} - C_{nb}^T C_b^T \hat{\lambda} C_b \quad C_s^T \hat{\gamma} C_{ss}] = W, \tag{18}$$

or, in compact matrix form,

$$\ddot{N} M_s + N K_s = W \,, \tag{19}$$

$$M_s = [C_{nb}^T (C_b^T \hat{J} C_b + C_r^T \hat{m}_b C_r) \quad C_{ns}^T \hat{m}_s] \,, \tag{20}$$

and

$$K_s = [C_s^T \hat{\gamma} C_{sb} - C_{nb}^T C_b^T \hat{\lambda} C_b \quad C_s^T \hat{\gamma} C_{ss}] \,, \tag{21}$$

where $\hat{\lambda} = -\hat{J}\hat{l}^{-2}\left\lfloor \dot{B}^T \dot{B} \right\rfloor - \frac{1}{2}\hat{l}^{-2}\lfloor B^T(W - S\hat{\gamma}C_s)C_{nb}^T C_b^T \rfloor$.

1.8 Class-k Tensegrity Systems

For tensegrity structures that have bar-to-bar connections, via joints or bearings, the previous dynamics can be simplified. Structures with these bar-to-bar connections are termed "class-k" systems, where the letter k denotes the maximum numbers of bars at a single node. For instance, a class 1 structure only has one bar at a single node, and thus there are no bar-to-bar connections. A class 2 structure will have a maximum of two bars at any given node (at least one node), and so on.

So, if there are two bars, one with endpoint (n_1) and one with endpoint (n_2) that are connected via a joint at these two respective nodes, it must be always true that n1 = n2. To achieve this constraint, the matrices P and D are specified such that

$$NP = D, \tag{22}$$

where P is a n-by-c matrix, and D is a 3-by-c matrix, n is the number of nodes and c is the number of constraints [5]. For any number of nodes to be held together, there must be some virtual force acting on the endpoints to secure the connection [5]. The constraining forces are defined as ΩP^T and thus the dynamics is redefined as

$$\dot{N}M_s + NK_s = \mathrm{W} + \Omega P^T, \tag{23}$$

and

$$\hat{\lambda} = -\hat{J}\hat{l}^{-2}\left\lfloor \dot{B}^T \dot{B} \right\rfloor - \frac{1}{2}\hat{l}^{-2}\lfloor B^T(W + \Omega P^T - S\hat{\gamma}C_s)C_{nb}^T C_b^T \rfloor \tag{24}$$

where Ω is a 3-by-c matrix of Lagrange multipliers that satisfies the constraints [5].

1.9 Reduced Order Dynamics

The last step in defining dynamic tensegrity systems is to correct for the reduction in degrees of freedom that are a result of the constraining forces [5]. Following the procedure outlined in Goyal and Skelton (2019), the class-k dynamics in matrix form are reduced to a smaller dimension via singular value decomposition (SVD) with two unitary matrices U_1 and U_2. [5]:

$$\ddot{N}UU^T M_s + NUU^T K_s = W + \Omega V \Sigma^T U^T \tag{25}$$

$$\rightarrow \ddot{\eta}_2 U_2^T M_s + \eta_1 U_1^T K_s + \eta_2 U_2^T K_s = W + \Omega V \Sigma_1^T U_1^T \ . \tag{26}$$

By performing post-multiplication of equation (25) with a non-singular matrix [U_2 M_s^{-1} U_1], the above dynamics can be expressed in two separate terms: the second order differential equations for the reduced dynamics, and an algebraic solution to the LaGrange multiplier [5]. The analytical LaGrange multiplier Ω can thus be found for any given system defined with K_s, $\hat{\lambda}$, and nodal matrices N_b and N_s [5].

1.10 Tensegrity Morphing Airfoils

Now that the dynamics of tensegrity systems is understood, structures can be built for many desirable shapes and applications. Once such example has been presented by M. Chen et al. (2020), a comprehensive study on tensegrity morphing airfoils using reduced order Class-k tensegrity dynamics and shape control law that is applicable to this thesis [3].

1.10.1 Error Bound Design of Airfoils

The procedure outlined by M. Chen et al. (2020) generates tensegrity NACA foil topologies via an error bound method as opposed to even spacing or cosine spacing methods [3].

The error bound method assumes each airfoil has length 1, and is discretized into several points [3]. In general, this error bound method estimates the exact curvature of an airfoil with many small straight-line segments, given that the deviation between the estimated straight line and actual airfoil curvature does not go above a specified value, or error bound [3].

The error bound procedure presented by M. Chen et al. (2020) specifies two coordinate points along the airfoil surface: (x_0, y_0) and (x_2, y_2), such that the line between the two points is

$$Ax + By + C = 0, \tag{27}$$

where $A = (y_2 - y_0)$, B = -1, and $C = (y_0 - Ax_0)$ [3]. When a line is drawn between these two points, there exists a point (x_1 , y_1) that has maximum distance from the actual airfoil surface

$$d = \frac{|Ax_1+By_1+C|}{\sqrt{A^2+B^2}}, \tag{28}$$

as defined in figure 1.6 [3]. Thus, each point (x_2, y_2) can be chosen depending on the desired error bound (i.e., the distance d) repeatedly across the length of the airfoil structure for each discretized point until the entire airfoil shape is generated.

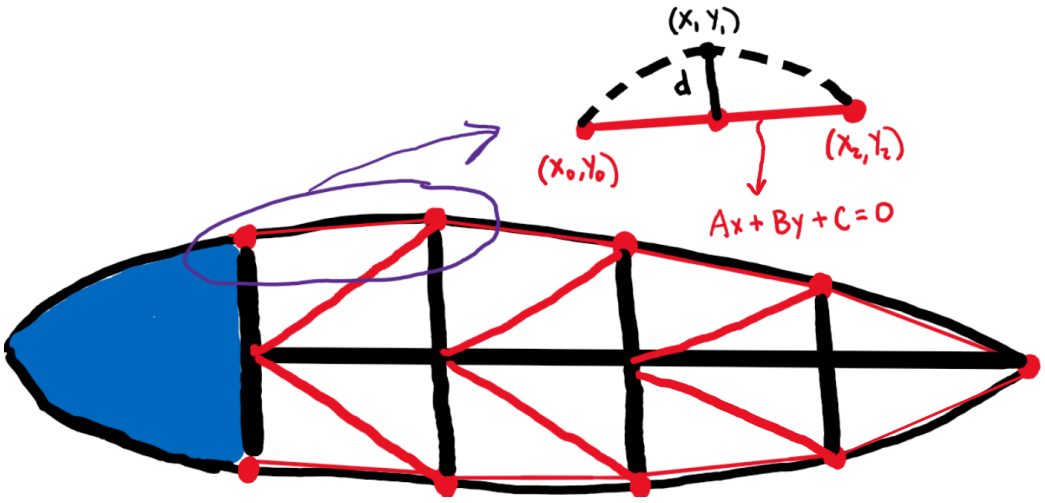

Figure 1.6. Error bound method for defining airfoil topologies. Inspired by [3].

As seen in figure 1.6, the airfoil can be split into a rigid head (in blue) and a dynamic trailing edge (tensegrity structure with red string and black bars). With rigid leading edge and morphing trailing edge, this airfoil is very similar to that of a carangiform fish that oscillates the trailing half of its body. Thus, motivation to utilize such structures to analyze swimming locomotion is evident and will be further discussed later.

1.10.2 Tensegrity Airfoil Connectivity Matrices

As for any tensegrity system, the nodal and connectivity matrices must be first defined before simulating a morphing airfoil. Depending on the complexity (q) of the tensegrity airfoil (i.e., the number of parallel, vertical bars within the morphing tail structure), the bar (C_b) and string (C_s) connectivity matrices are defined by

$$C_{b_{in}} = \begin{cases} [i, i+1], & 1 \leq i \leq q \\ [i-q, i+1], & q+1 \leq i \leq 2q \\ [i-2q, i+1], & 2q+1 \leq i \leq 3q \end{cases} \tag{29}$$

and

$$C_{s_{in}} = \begin{cases} [i+1+q, i+2+q], & 1 \le i \le q-1 \\ [2q+1, q+1] & \\ [i-q, i+2], & q+1 \le i \le 2q-1 \\ [i-2q+1, i+3], & 2q \le i \le 3q-2 \\ [i+3-q, i+4-q], & 3q-1 \le i \le 4q-3 \\ [3q+1, q+1] & \end{cases}, \tag{30}$$

in which the two elements in each row represent the two end nodes of a bar or string segment [3].

Later in this thesis, a study on a morphing airfoil with topology modeled from the body geometry of a dolphin will be conducted to show the applicability of the shape control outlined by M. Chen et al. (2020) to arbitrary tensegrity systems and high angles of attack.

1.11 Information Architecture and Control

Tensegrity systems should be designed and optimized depending on the specific application, dynamic performance, and desired precision of the sensors and actuators used within the configurations, commonly referred to as information architecture. Goyal et al. (2020) present a method to simultaneously design the structure, information architecture and control for tensegrity systems [6]. In tensegrity control, linear matrix inequalities (LMIs) are generally used to bring the system into stability and satisfy the constraints of the input and control covariance [6]. However, by solving all three parameters of structure, architecture and control law, the problem becomes nonlinear, thus requiring nonlinear matrix inequalities to be convexified [6]. The convexifying LMI process is achieved by defining a nonlinear matrix inequality that holds the necessary conditions needed to redefine the system as a convex problem [6].

The method presented by Goyal et al. (2020) is useful in conducting cost-benefit tradeoff analyses between budget, prestress of strings, and precision of sensors/actuators. In other words, through a covariance upper bound procedure, one can determine whether more money should be

directed toward optimizing prestress conditions, or whether it is more beneficial to increase the budget for higher precision sensors/actuators in each string and node [6]. In such studies, the free structure parameter is the tensegrity dynamics with specified string pretension, the control input is string force density, and the outputs are initial prestress of each string, the precision of sensors and/or actuators, and the dynamic controller characteristic matrices [6]. One such example found that for a desired performance and control constraint, the strings directly responsible for the motion of specified nodes will require higher precision than strings not immediately in control of said motion, as would be expected [6]. Other tradeoffs can be conducted such as between total budget and output bounds to monitor the change in required input constraints, where relaxing the output constraint and increasing the budget are both found to result in decreasing input requirements [6].

CHAPTER II

MOTIVATION FOR TENSEGRITY SWIMMERS

Low propulsion efficiencies resulting from wakes, drag and turbulence—as experienced in submarines—are less of a problem for fish and aquatic mammals that, after evolving for millions of years, have become the fastest and most efficient swimmers on Earth [7]. By flexing through the water with harmonic tail and fin motions, fish experience less than half the amount of drag that would be experienced if the same rigid bodies were simply towed through water [7] [8] [9]. Thus, the desire to re-design underwater vessels with biomimetic principles has shaped much of novel research and development within naval engineering fields.

2.1 Past Work on Swimming Kinematics

As early as the 19th century, the distinctive locomotion styles of different fish species have been of great interest within the field of zoology. In 1873, marine biologist William Saville-Kent set the stage for defining the term we know as swimming gaits, or vibrational modes, of various fish. Saville-Kent published an article in Nature describing different shark species by fin size, tail beat frequency and amplitude, and the resulting swimming performance [10]. Saville-Kent also marked the major differences between shark and fish species, where some fish tend to rely more on pectoral fins for locomotion rather than simply rotational stabilization as do sharks [10]. Understanding the mechanical principles that allow for these various swimming performances is crucial for designing underwater vehicles with broad applicability, from underwater surveillance, high-speed travel and transportation, coral regeneration, and much more. At the turn of the century, fish locomotion became a significant interest to physicists and mathematicians, not just zoologists.

In the 1930s, Dr. J. Gray found that despite noticeable differences between the swimming motion of eels, fish, and dolphins, the general concept for all harmonic swimming animals is a result of a similar muscle contraction wave traveling down the length of the body [11]. As each muscle contracts, the surface of the fish body moves transversely to the direction of motion to produce forward thrust [11]. Although Gray did not define the equations for calculating this forward thrust, he suggested it was a function of the angle between the fish surface and its line of motion, as well as the velocity of the transverse motion [11]. This "muscular wave" theory would later motivate many kinematic theories regarding thrust production in swimming bodies.

Throughout the 1960s, M.J. Lighthill defined his "elongated body" theorem in hopes to explain how anguilliform swimming fish, most often much longer in the direction of travel than they are wide, can achieve high swimming performance via small movements in the direction perpendicular to the forward travel direction [12]. Lighthill defined the lift force of an oscillating fish body to be equal to the change in momentum of fluid passing through the cross section of a cylinder [12]. It was concluded that the average thrust generated for a swimming body is calculated by subtracting the kinetic energy lost in the wake from the work generated by the lift forces as:

$$P = 0.5\rho A\{\left(\frac{dz}{dt}\right)^2 - U^2\left(\frac{dz}{dx}\right)^2\} \tag{31}$$

where the transverse tail motion is in the z-direction, forward motion in the x-direction, P is the mean thrust, ρ the density of the cylinder, A the cross-sectional area and U the current in the x-direction flowing past the fish [12].

By the end of the 1970s, Lighthill had begun generalizing his initial theory to include fish swimming at variable tail beat amplitudes, such as for carangiform and thunniform swimming

fish and marine mammals, where only the posterior third of the body moves [13] [14]. By oscillating the caudal fin and peduncle, instead of generating a wave along the entire body as in anguilliform swimming, Lighthill suggested the carangiform mode to have higher efficiency in thrust production by taking advantage of reactive forces via a quick rate of change of momentum between the tail and the water mass [13] [14].

As a result of over a century of swimming kinematic research, it became understood that the design flaw preventing conventional underwater vehicles—such as submarines and submersibles—from achieving high efficiency propulsion is that they are not conforming structures. Rather than flexing and controlling vorticity in response to oncoming currents and eddies, these rigid vessels must plow through the water all while generating wide wakes, large drag coefficients and high turbulence [7].

2.2 Review of Past Robotic Swimmers

The nature of muscle contractions used for swimming is different for every species, and thus for building underwater robotics, the size and function of the vessel will determine which swimming gait is desired to mimic. Lighthill's study on the simplified dynamics and increased thrust production in thunniform swimmers has motivated novel experiments in producing biomimetic tuna and dolphin robots.

Triantafyllou & Triantafyllou (1995) present a robotic Tuna composed of metal vertebra linked via hinges that are actuated by various tendons, pulleys, and several motors [9]. The internal machinery is enclosed within an elliptical rib-like case and encapsulated within a flexible, foam-Lycra skin such as used in diving wetsuits. The rib-like structure allows the fish body curvature to closely mimic the tuna body while the foam-Lycra composite skin is smooth

and durable enough not to deform or dip below each rib-like beam [9]. As the fish tail oscillates, the elliptical ribs bend to give steady structural support to the encapsulating skin. Pressure, force, and motion sensors/traducers are placed along the outside skin of the dolphin to monitor swimming performance.

Yu et al. (2011) present a robotic dolphin composed of a metal skeleton and flexible, waterproof skin. A pitch joint in the neck allows for a change in angle of attack by distributing the weight of a cylinder on a moving slide [15]. In addition, pitch change is also achieved via asymmetric thrust production in up/downstrokes [15]. A yaw joint connecting the rigid forebody to the oscillating caudal section is responsible for turn maneuvers [15]. Yu et al. (2011) also address the anti-corrosion and anti-fouling properties of the internal members that are fully submersed in water, a conversation notable for submersibles that will operate in corrosive environments for long periods of time.

Yu et al. (2016) later offer a very realistic dolphin capable of leaping out from the water surface as seen in nature. The 90W motor is chosen by calculating the expected average power generated from the tail to reach the necessary leap velocity [16]. Parts are made as light as possible, and include aluminum and titanium structural parts, polypropylene (PP) airfoil fins, and lactoprene skin. The measured frequency and velocities are in agreeance with that found in Tanaka (2019) for a real dolphin during leaping motions [17]. The use of multiple motors (one per joint) makes high thrust generation possible within the robotic dolphin, however, requires more space to be used for batteries to achieve long operation periods. Due to the swimming gait of thunniform swimmers (such as dolphins and tuna), the space needed for electronics is satisfied by the smaller ratio of dynamic to static body dimensions than is in anguilliform swimmers.

Despite the possible advantage in thrust production and mechanical design of modeling thunniform swimming modes, extensive research has been devoted to a wide range of swimming gaits, such as carangiform and anguilliform. Chen and Jiang (2019) built a tensegrity carangiform swimmer with swimming performance close to that of common carangiform fish at Strouhal numbers near 0.5 [18]. The tensegrity backbone design allows for the anisotropic bending stiffness of the spinal column to be precisely controlled for biomimetic applications [18]. Chen and Jiang (2019) further note that the use of tensegrity theory for robotic swimmers is useful in optimizing the bending stiffness of each vertebra separately, in order to optimize swimming performance [18].

Wen et al. (2012) published a paper exploring the relative swimming performance of all three undulatory kinematics (anguilliform, carangiform, and thunniform) applied to a single Mackerel inspired robot. The results of this study suggest that the thunniform swimming gait is most capable of reaching high speeds (St = 0.424), while carangiform is the second fastest (St = 0.43), and anguilliform the slowest (St = 0.55). This comprehensive study further suggests the validity of Lighthill's elongated body theory from the early 1970s in which it was predicted that carangiform gaits are more efficient in producing thrust than anguilliform gaits [13] [14] [19].

CHAPTER III

DOLPHIN BIOMIMETIC PROPERTIES

The design of the robotic dolphin in this paper begins with the analysis of biomimetic properties of real dolphins, including body geometries, swimming gaits and corresponding muscular and spinal anatomies that will be desired to replicate.

3.1 Dolphins Throughout History

The great swimming performance and elegance of dolphin species has always been understood throughout history. However, before the development of the mathematical models, the true physics behind the efficiency of dolphin swimming was not understood, and thus broad claims about dolphins have been made throughout history. For example, Aristotle, in his Historia Animalium from 350 BC, wrote that dolphins were the fastest swimming marine animal and could even jump over the top of ships [20]. Aristotle also believed that dolphins could produce human vowels [20].

Another historical misunderstanding of dolphin performance is Gray's paradox. After observing a dolphin swimming alongside of a ship, Gray predicted the swimming velocity and compared the required swimming power to the ability of muscles to preform work, concluding the muscles of the dolphin could not physically produce enough power to swim at such speeds. However, his estimation of necessary muscle power was from the long duration performance of an oarsmen, while the dolphin he observed was swimming in a short burst [20].

3.2 Body Shape of Dolphins

Tanaka et al. (2019) generated a 3-dimensional image of a Pacific white-beaked dolphin by 3D scanning a frozen corpse and correcting the deformed body to have perfect symmetry within fins and along the length of the body, as seen in figure 3.1 [17].

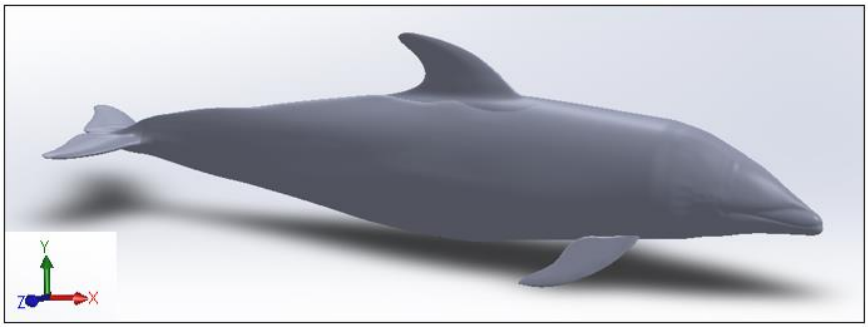

Figure 3.1. SolidWorks model of dolphin [17].

Using the above the CAD model, evenly spaced surface polynomials are generated along the length, width and height of the dolphin body, excluding the fins, as shown in figure 3.2.

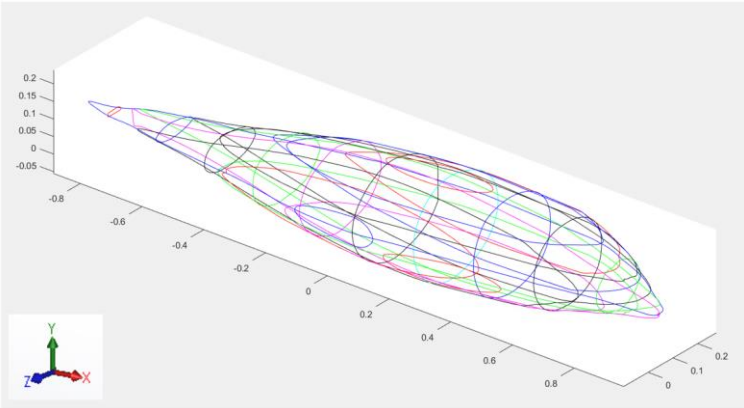

Figure 3.2. Polynomial curves generated across the dolphin body without fins. Units in meters.

The polynomials in figure 3.2 allow for the dolphin surface coordinates to be defined, which will be necessary for later methods such as modeling the tensegrity spine structure and specifying the tail dynamics. For example, the tensegrity nodes (N, S, B) as well as the

connectivity matrices (C_s, C_b), as discussed in chapter 1, will be defined along these polynomial surface curves to generate a tensegrity model that mimics the dolphin body.

3.3 Anatomy of Common Dolphin Species

Spinal anatomy is referenced for sake of biomimetics. Long (1997) conducted extensive research on biomechanics and morphology of saddleback dolphins, outlining the bending stiffness of various vertebra along the caudal region of backbone [21]. It was found that just aft of the dorsal fin, the bending stiffness is roughly 55 Nm/rad, while within the pre-fluke region, bending stiffness is <1 Nm/rad [21]. Inspired by the work of Chen and Jiang (2019) to model each vertebra separately, this thesis utilizes the anatomy of real dolphins to apply the relative bending stiffnesses found in previous studies along the backbone of the robotic dolphin.

3.4 Swimming Kinematics and Thrust production

Most dolphin species swim with an amplitude roughly equal to 20% of their body length, which stays constant for slow and fast swimming velocities [16] [22] [23] [24]. This constant amplitude allows for simple control of the tensegrity system that will not have to achieve multiple up/downstroke configurations for different swimming velocities.

The angle of attack of the tail fluke has been found to follow a sinusoidal motion during forward swimming and reaches angles of approximately zero at the end of each up/downstroke. At the start of each stroke (i.e., after maximum amplitude has been reached and opposing motion begins), the tail fluke is deflected by hydrodynamic forces (up to a maximum angle of $\sim\pm35^{o}$ [22]) due to the very low stiffness of the pre-fluke vertebrae [21]. This property is crucial so that fluid is pushed behind the dolphin to produce forward thrust.

As pointed out by Pabst (1992) the muscles responsible for producing movement in dolphins are very different from those commonly seen in mammals [25]. For example, while humans rely on appendicular tendons to produce movement in hands, arms, feet and legs, Cetaceans, rely on axial muscles for swimming [25]. Pabst (1992) suggests the primary epaxial muscles used for the upstroke are the m. multifidus and the m. longissimus that travel along the top portion of the vertebrae from the head all the way along the spinal column [25].

Thrust production is also a byproduct of the high-aspect tail fluke with airfoil cross-section that generate hydrodynamic lift [22]. The cross-sections of a Pacific white-beak's fluke, dorsal fin, and pectoral fin, gathered by Tanaka et al. (2019), can be seen in figure 3.3.

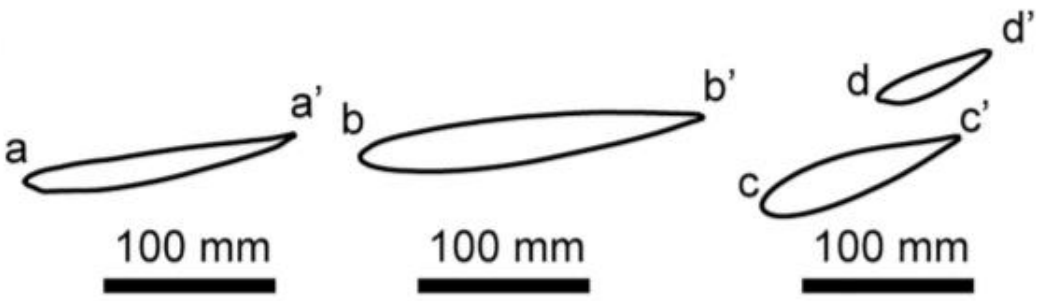

Figure 3.3. Cross sections of the pectoral (a-a'), dorsal (b-b'), and fluke (c-d', d-d') fins [17].

Guo et al. (2020) found that a significant portion of the thrust production in swimming dolphins is a result of the oscillating tail fluke, producing up to 4x as much thrust during each up/downstroke as the rest of the flexing tail section [26]. The airfoil cross-sections of the other appendages, such as the dorsal and pectoral fins, also give rise to boundary layer and flow separation phenomena that will be discussed later.

Lastly, it is beneficial to analyze the geometry of dolphin bodies and appendages in a similar method used to analyze the stability of submarines and surface vessels. One important

property of dolphins is that they are neutrally buoyant, which offers them great maneuverability to either surface for oxygen, or dive deep to chase prey. The pectoral fins are less responsible for motion, but operate like Bilge keels for ships, giving roll stabilization. Another important variable that affects stability is the center of mass, which for the provided CAD model is given in figure 3.4.

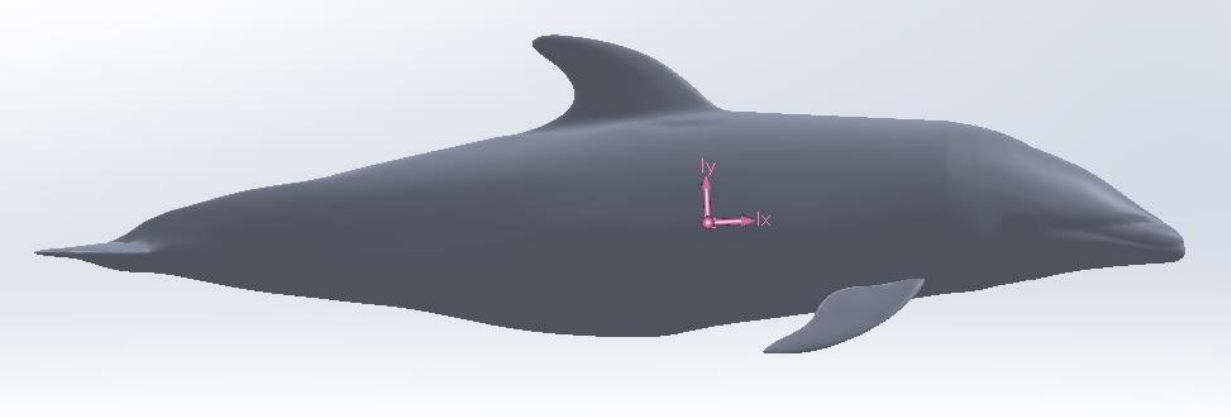

Figure 3.4. Center of mass of a dolphin. CAD model from [17].

The center of mass in figure 3.4 assumes constant body density and is consistent with data provided in previous literature for the center of mass of real dolphins [27].

CHAPTER IV

METHODS OF MODELING THE TAIL AND DOLPHIN BODY

4.1

The tail structure is designed as both a 3D printed physical model to be tested in a swimming tank, and as a computational tensegrity model that can be used for feedback control in the future. Note that the CAD model from figure 3.1 is decimated to 0.5 from the original model (using Blender) to reduce the number of faces to allow the model to be opened in SolidWorks in a reasonable amount of time.

4.1.1 2D Tensegrity Tail

In figure 4.1, a dynamic tensegrity model of the dolphin is generated using a MATLAB code originally used to control the dynamics of morphing airfoils [3].

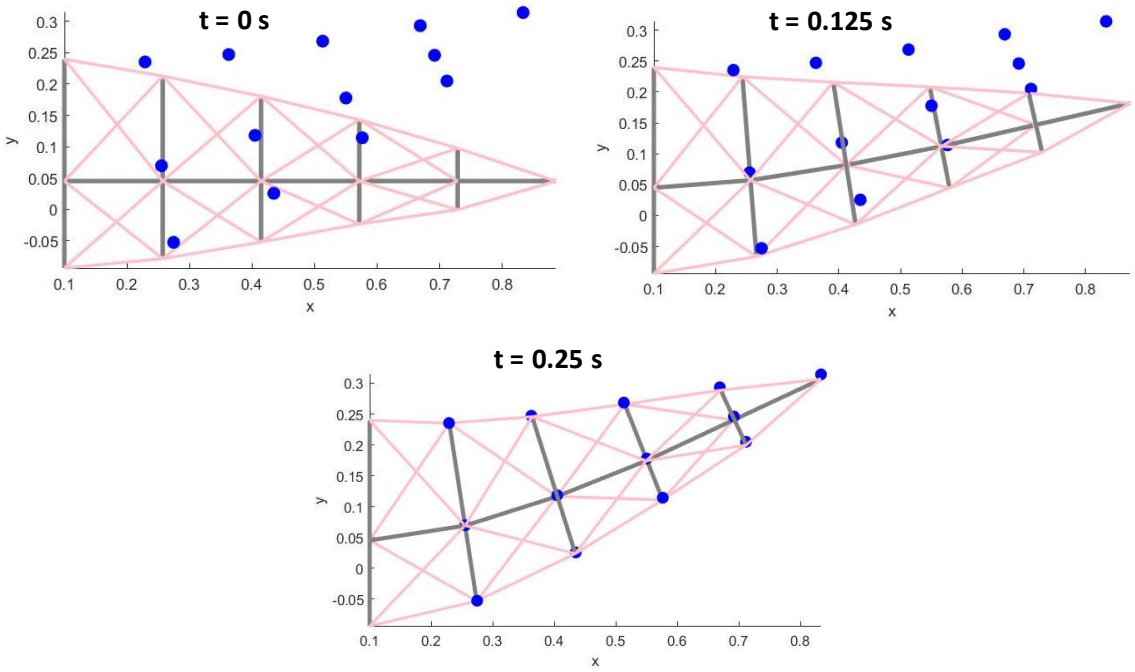

Figure 4.1. 2D morphing dolphin tail.

In figure 4.1, the blue dots represent target nodes to be achieved by altering the angle between each of the horizontal bars. Note that this model does not include the tail flukes, but simply the flexing caudal portion of the body. The bar members can be thought of as the rigid vertebrae, with strings acting as the actuating muscles along the spinal column responsible for movement. During upstroke motion, string and bar lengths are monitored and can be seen in figure 4.2 and figure 4.3, respectively.

(a)

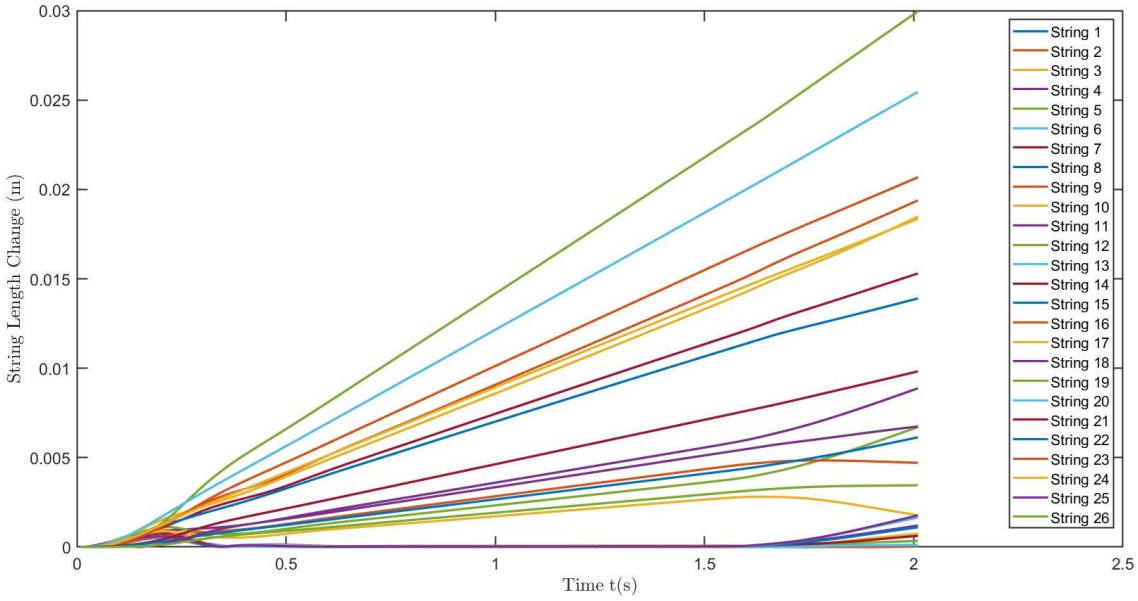

(b)

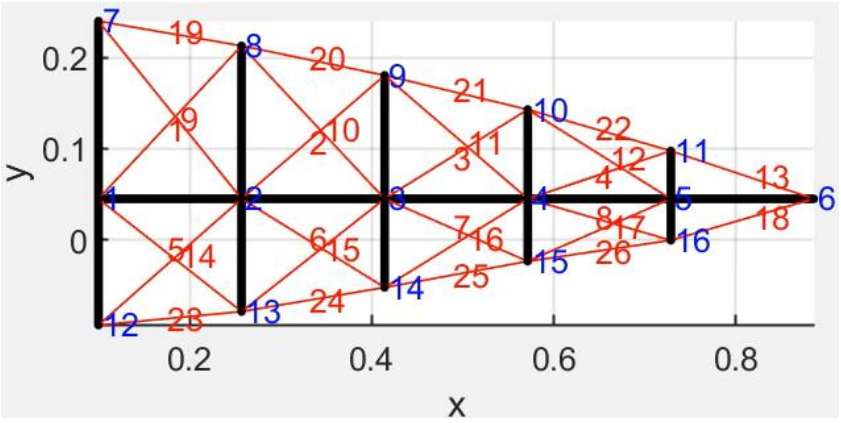

Figure 4.2. (a) String length change of morphing tail. (b) String and node number labels. (b) String and bar numbering in red and blue, respectively.

(a)

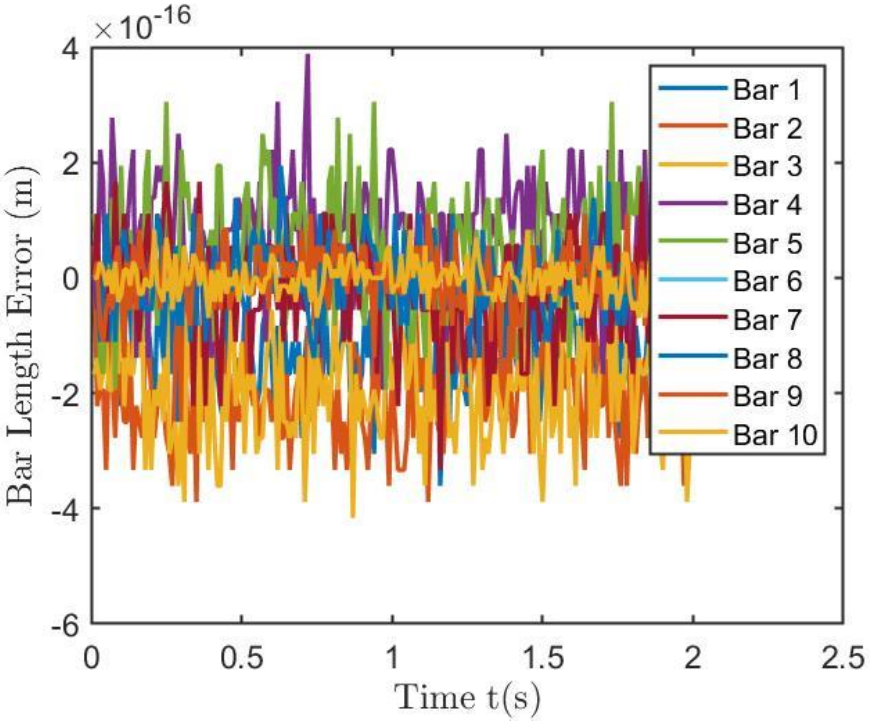

(b)

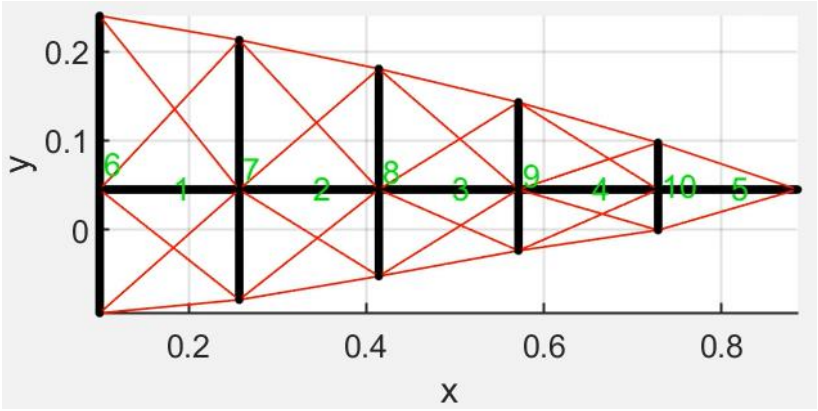

Figure 4.3. (a) Bar length error. (b) Bar numbers in green.

4.1.2 3D Tensegrity Tail

The 2D tail structure outlined in 4.1.1 only advances the design of morphing 2D airfoils but limits the tensegrity applications for thrust production. A 3D model, as seen in figure 4.4, can be used for complex control of the bending tail and analysis of hydrodynamic forces.

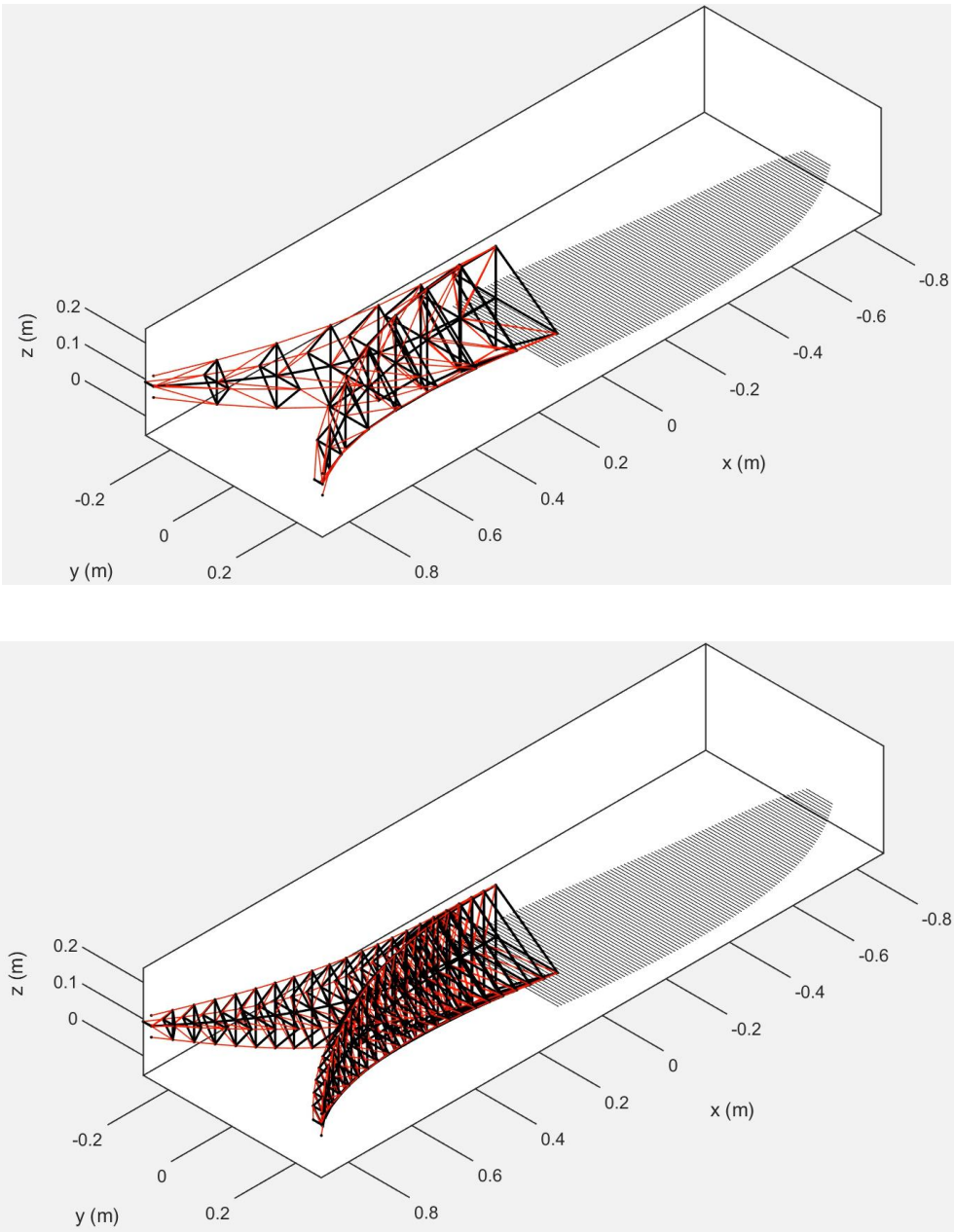

Figure 4.4. 3D tensegrity tail strokes at backbone complexities q = 7 (top) and q = 21 (bottom).

As with tensegrity airfoils and other structures, the tensegrity tail can be designed with any given complexity (q), where complexity defines the number of vertical bar members. Typical dolphin species have 22 vertebrae within their caudal region [21] [25], and thus the tail

structure given in figure 4.4 with complexity q =21 is more biomimetic in nature, and represents a more continuous body surface, as opposed to a complexity of q = 7.

4.2 Physical Tensegrity Tail

The 3D model from Tanaka et al. (2019) is scaled by 30% to allow for the dolphin to swim freely in a medium size tank. In future work, if a central pattern generator were to be used to train certain swimming gaits, the robot would not need a large area to swim steadily, accelerate, leap and so forth, as would be needed at full scale. Thus, with a vessel length of 0.55m, this design-stage robotic dolphin is realistic for a wide range of applications.

There are two tail structures analyzed in this thesis: a tail with four intervertebral joints (complex tensegrity structure) and a tail with two intervertebral joints (simple tensegrity structure). To design each tail, the trailing 1/3 end of the dolphin is designed with simple hinges at each intervertebral joint and printed with PLA. The density of PLA is 1.24 kg/m^3, and thus to reach neutral buoyancy, keeping in mind the added mass from the servomotor and skin material, the parts are printed with a volumetric infill of 70%. The printed models are compared in figure 4.5.

(a)

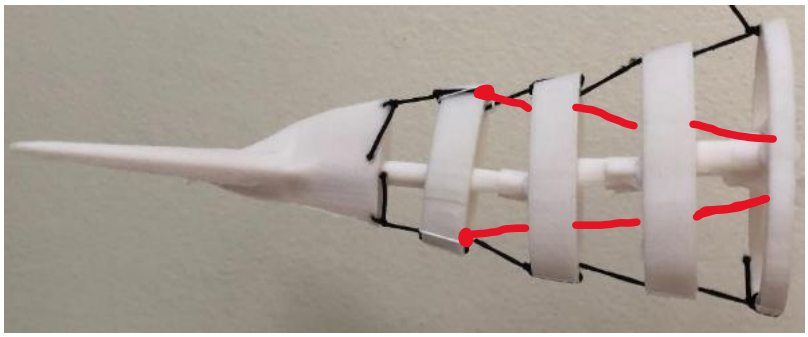

(b)

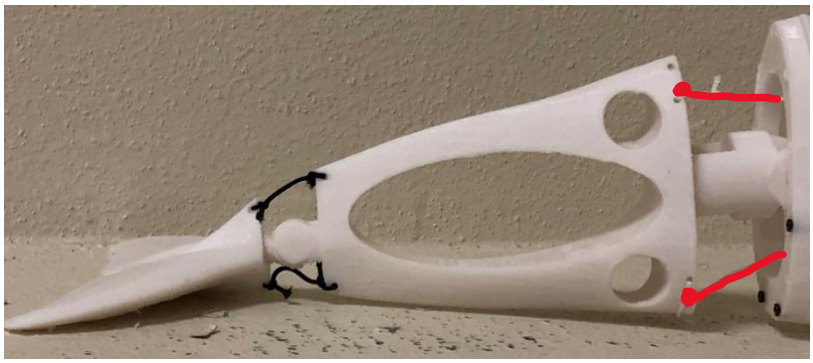

Figure 4.5. (a) Complex tail with 4 joints. (b) Simple tail with 2 joints.

In figure 4.5 (b), holes within the caudal region are made to reduce mass, and thus reduce the torque required by the servo motor for actuation. The black elastic bands hold tension between each respective vertebra and are meant to mimic the axial muscles responsible for caudal extension, such as the m. multifidus and m. longissimus discussed in Pabst (1993) [25]. Since it is known that the bending stiffness in general reduces from dorsal fin to flukes, each black string in the complex structure is given a relative pretension to match that found in Long et al. (1997) [21]. The simple structure cannot be modeled with variable bending stiffness, but still utilizes a fluke joint with the desired low bending stiffness [21].

The two red strings in figure 4.5 are connected to the motor and are responsible for the actuation of the tensegrity tail structure. Note that the actuating strings for the complex design are not attached to the flukes, but just forward of them, as to allow the flukes to follow the

desired angle of attacks during swimming. Figure 4.6 shows the actuating system including the motor, which oscillates between $\pm 45^{o}$, and the Spectra fiber strings for the simple design.

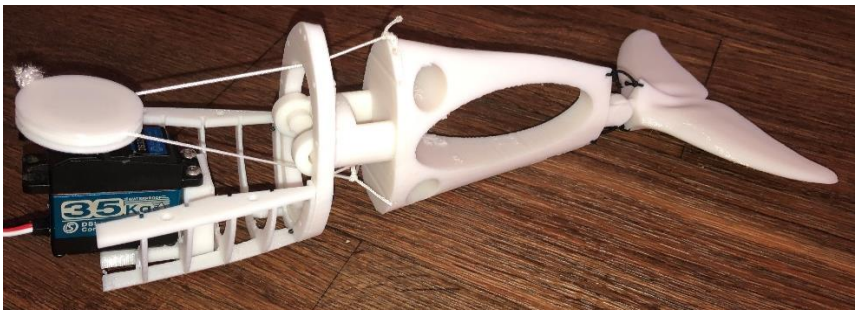

Figure 4.6. Actuating mechanism.

4.3 Hull Profile of the Dolphin Head and Midsection

Unlike the caudal third designed as the previously discussed tensegrity structure, the rigid head is designed as a static structure of parallel plates. However, because no dynamic control is needed in the front 2/3 of the body and head, all plates are connected by horizontal beams forming a body and head cage for the skin material to rest on top of. The fully assembled dolphin robot with tail, mid-body and head are given in figure 4.7.

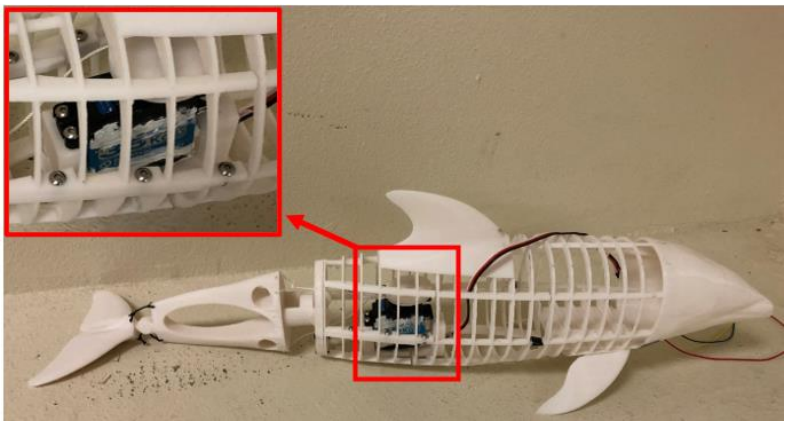

Figure 4.7. Assembled robot with servo attached to motor mounts. Servo additionally waterproofed with caulk.

As noted earlier, it is important to replicate the neutral buoyancy and center of mass location for a real dolphin to have the same stability and maneuverability. The center of mass of the CAD models can be seen in figure 4.8.

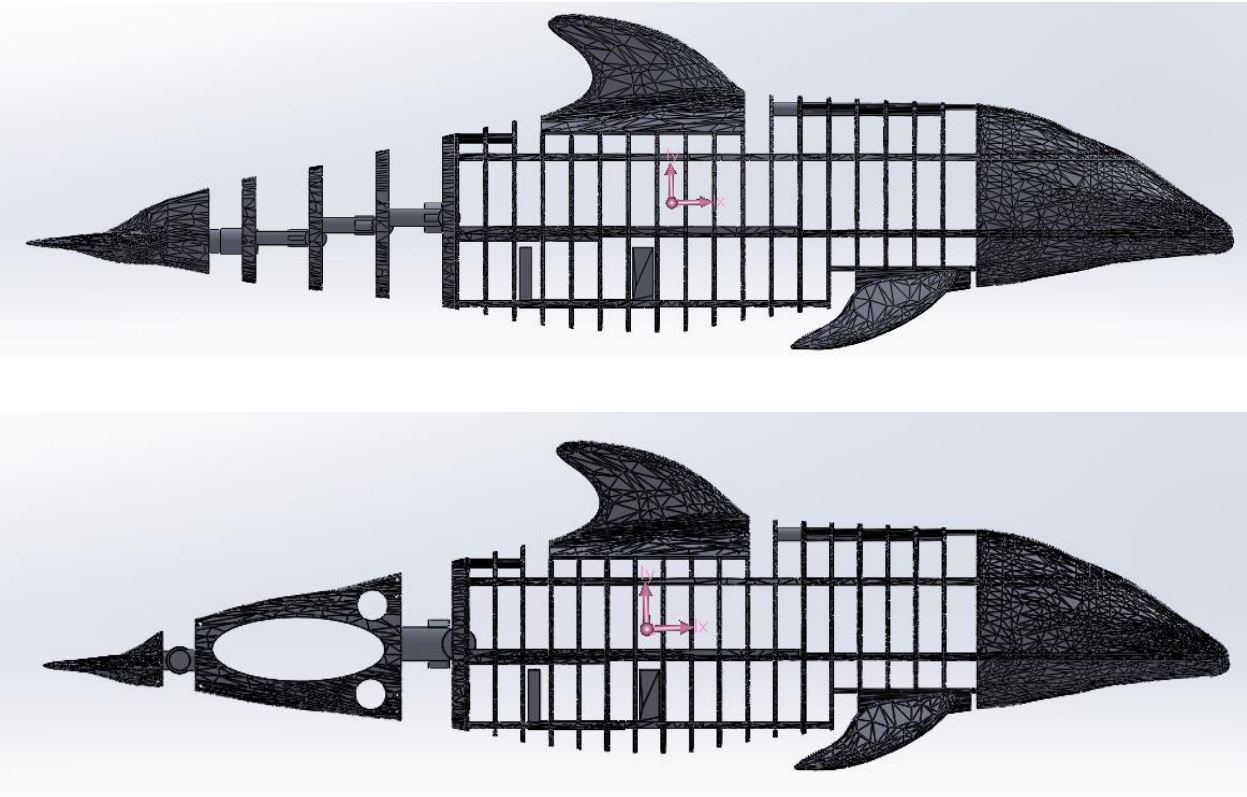

Figure 4.8. Center of mass (pink origin) of the tensegrity dolphin for the complex (top) and simple (bottom) tail structures.

The above center of mass locations do not include the additional mass of the motor assembly. Upon addition of the motor to the motor mount, the center of mass locations will both shift further aft, and thus additional mass added near the leading edge of the dolphin will be expected to move the center of mass closer to that of a real dolphin, as in figure 3.4.

To produce thrust more efficiently, the tensegrity tail must be covered with a flexible skin as seen in figure 4.9. The material used is a Lycra-foam (neoprene) skin material, and is the most

common material used in scuba wetsuits due to its waterproof properties, meaning that for the robotic dolphin, will be able to displace water during up/downstrokes.

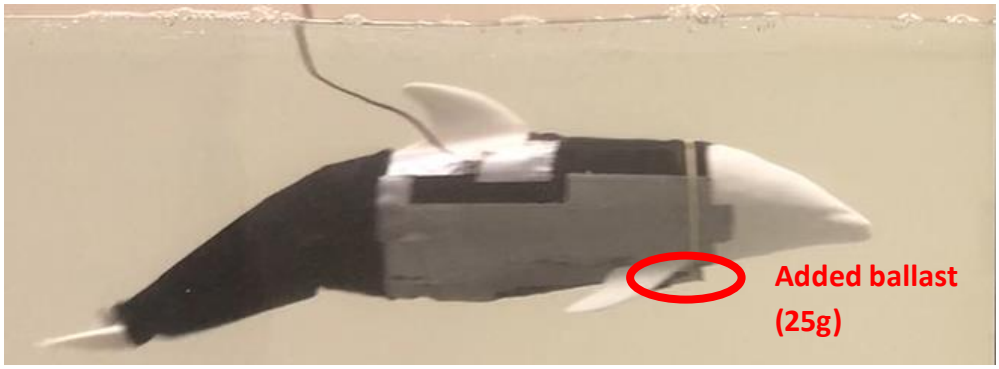

Figure 4.9. Assembled dolphin body in water with external electronics.

The motor is placed just forward of the tail structure. A small metal weight of 25g is placed forward of the pectoral fins to reach natural buoyancy and pitch stabilization. Note that in this presented thesis the electronics, besides the servo motor, are external for purposes of testing the swimming ability with ease before waterproofing the electronics. However, there are mounts above the pectoral fins where the electronic housing can be placed as seen in figure 4.10.

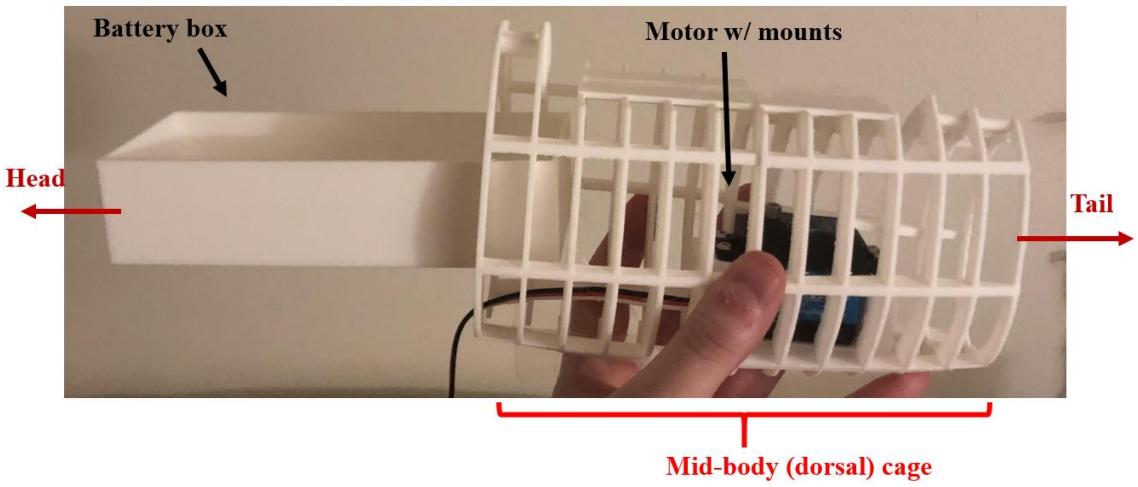

Figure 4.10. Electronic housing within the head section.

The scale of the dolphin was chosen such that the head and mid body would be as small as possible while still capable of holding the Arduino controller, batteries, and all necessary wiring for future studies. The dimensions of the robotic dolphin are given below in table 2.1. Width is measured at maximum width and does not include the pectoral fins. Height is measured vertically downwards from the highest point of the dorsal fin.

Table 2.1. Robotic dolphin physical dimensions.

Length (m)	0.55
Width (m)	0.088
Height (m)	0.15
Projected area (m^2)	$8.376760e^{-3}$
Volume (m^3)	0.00202

CHAPTER V

CFD SIMULATION METHODS

Tanaka et al. (2019) conducted CFD analyses of the pressure and wall shear stress distribution along the dolphin body as it glides through water in a straightened position. The simulations were of high Reynolds number flows, used to replicate the hydrodynamics of a burst-swimming and leaping dolphin [17]. In this paper, similar simulations are conducted to gather data at low Reynolds numbers at swim speeds of common, steady swimming dolphins. The model is 3-dimensional, implicit unsteady with turbulent flow, ran within STAR-CCM+ with a generated mesh of 7.5 million total elements. The flow is segregated, as opposed to coupled, to save computational cost and run properly on a 4-core i7 Lenovo Yoga laptop. Each simulation is solved over 180 time-steps with 5 inner iterations. In this section the physics of the models are defined. The dolphin body is again scaled to 30% of the original model to match the dimensions of the robotic dolphin.

5.1 Equations of State

First, the model is defined with constant density $\rho = \rho_0$ equal to that of water at room temperature as set by default for liquid flows in STAR-CCM+ [28]. The density of H_2O is 997.561 kg/m^3[28]. Kinematic viscosity for water at 23°C is $9.345e^{-7}$ m^2/s [17].

5.2 Boundary Conditions

The velocity inlet is given constant values of 1-4 BL/s, where BL is the body length of the dolphin, to mimic the typical gliding velocities of common dolphin species as noted throughout literature. Simulations were also conducted at high Reynolds number velocities to compare to Tanaka et al. (2019) to determine replicability [17] [21] [22] [24]. Testing at these

higher Reynolds numbers may also be applicable to high-speed vessels or submarines that utilize the biomimetic geometries of dolphin bodies.

Both the velocity inlet and pressure outlet are specified as boundary normal, meaning the fluid flow is orthogonal and opposite to the swimming direction [28]. The pressure outlet is given a constant value of 0.0 Pa. At the outer domain of the fluid flow, the boundary is considered a symmetry plane with all normal velocity, gradients, and mass flux equal to zero [28].

5.3 Turbulence

A Reynolds-Averaged Navier Stokes (RANS) turbulence model is used by defining energy, velocity and pressure as composed of mean ($\bar{\Phi}$) and fluctuating components (Φ') as

$$\Phi = \bar{\Phi} + \Phi' \tag{32}$$

To derive the universal laws of conservation for generic fluid dynamics, the 3-dimensial coordinate systems (x1, x2, x3) is used to define a fixed volume **V** with surface d**V** within a fluid as seen in figure 5.1.

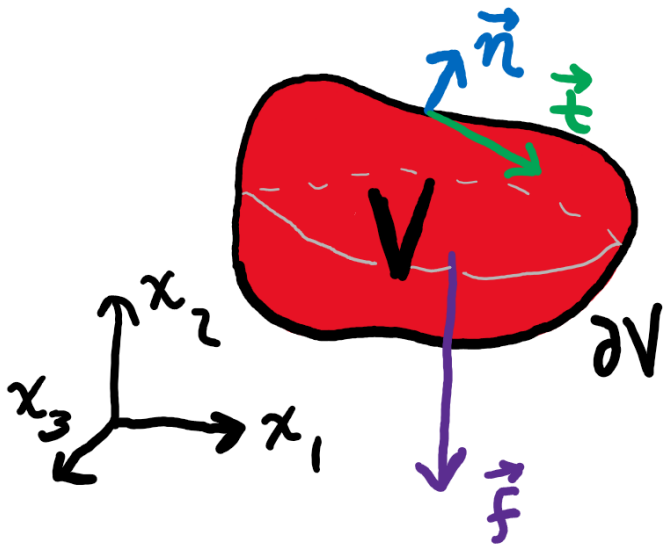

Figure 5.1. A body composed of mass points each experiencing body forces (**f**) and surface forces/tractions (**t**) in 3D space. The vector **n** represents the normal direction pointing away from the body. Derived in [29].

Mass continuity is derived from the fact that the mass accumulated within the volume **V** must cancel the mass flux through the partial derivative $\partial \boldsymbol{V}$:

$$\int \frac{\partial \rho}{\partial t} d\boldsymbol{V} + \int \rho v_i n_i dS = 0, \tag{33}$$

where v_i is the velocity component, n_i is the normal vector, ρ is the constant density of water, and dS is a surface integral [29].

Substituting with the divergence theorem, mass continuity becomes

$$\frac{\partial \rho}{\partial t} = \nabla \cdot (\rho \bar{v}) = 0, \tag{34}$$

where $\bar{v}$ is the mean velocity [28] [29].

For conservation of linear momentum, the rate of change of linear momentum within a body is balanced by the momentum transferred via body forces and the flux of momentum across the body boundary [29]. We define rate of change of linear momentum equal to the summation of all tractions on the body surface, the body forces, and the outward flux (negative) of momentum:

$$\int \boldsymbol{t} ds + \int \rho \boldsymbol{f} dV - \int \rho \boldsymbol{v}(\boldsymbol{v} \cdot n) ds \; = \int \frac{\partial(\rho \boldsymbol{v})}{\partial t} dV. \tag{35}$$

With the use of Cauchy's formula ($t_i = \sigma_{ji} n_j$), divergence theorem and considering an arbitrary volume V, conservation of linear momentum in coordinate invariant form is

$$\nabla \cdot \sigma + \rho \mathbf{f} = \rho \frac{D\boldsymbol{v}}{Dt} = 0. \tag{36}$$

Similarly, conservation of angular momentum states that the rate of change of angular momentum within a body is balanced by the angular momentum due to body force moments and angular momentum flux through the body boundary [29]. This balance is mathematically achieved by a symmetric stress tensor, where at every point in the body volume and boundary

$$\sigma_{ij} = \sigma_{ji} \tag{37}$$

Conservation of energy follows from the equality DU/Dt + DK/DT = DW/DT + DQ/DT where U, K, W and Q are internal energy, kinetic energy, work done on the region, and heat added to region, respectively [29]. It then follows by definition,

$$\int \rho u \; d\boldsymbol{V} + \int 0.5 \rho v_i v_i \; d\boldsymbol{V} = \int \rho f_i v_i \; d\boldsymbol{V} + \int t_i v_i \; dS - \int q_i n_i \; dS + \int \rho r \; d\boldsymbol{V}, \tag{38}$$

where u is the internal energy per unit mass ($= \lim_{\Delta V \to 0} \frac{dU}{p\ dV}$), t_i the surface traction, f_i the body force, r the internal heat per mass term such as microwave radiation, and q_i is the heat flux vector (energy per unit area per time).

In STAR-CCM+, mean momentum and energy transport are defined with the stress tensor term T_{RANS}:

$$\frac{\partial}{\partial t}(\rho \bar{\boldsymbol{v}}) + \nabla \cdot (\rho \bar{\boldsymbol{v}} \otimes \bar{\boldsymbol{v}}) = -\nabla \cdot \bar{p}\boldsymbol{I} + \nabla \cdot (\bar{\boldsymbol{T}} + \boldsymbol{T}_{RANS}) + \boldsymbol{f}_b, \tag{39}$$

$$\frac{\partial}{\partial t}(\rho \bar{E}) + \nabla \cdot (\rho \bar{E} \bar{\boldsymbol{v}}) = -\nabla \cdot \overline{pv} + \nabla \cdot (\bar{\boldsymbol{T}} + \boldsymbol{T}_{RANS})\bar{\boldsymbol{v}} - \nabla \cdot \bar{\boldsymbol{q}} + \boldsymbol{f}_b \bar{\boldsymbol{v}}, \tag{40}$$

$$\boldsymbol{T}_{RANS} = -\rho \begin{pmatrix} \overline{u'u'} & \overline{u'v'} & \overline{u'w'} \\ \overline{u'v'} & \overline{v'v'} & \overline{v'w'} \\ \overline{u'w'} & \overline{v'w'} & \overline{w'w'} \end{pmatrix} + \frac{2}{3}\rho k \boldsymbol{I}, \tag{41}$$

where $\bar{p}$ is mean pressure, **I** the identity matrix, $\bar{\boldsymbol{T}}$ the mean viscous shear tensor, $\boldsymbol{f}_b$ the body forces of gravity and centrifugal forces, $\bar{E}$ the mean total energy per unit mass, $\bar{\boldsymbol{q}}$ the mean heat flux and k the turbulent kinetic energy [28].

5.4 Turbulence Models: k-ω and k-ϵ

Simulations are done using the SST k-omega method presented by Menter (1994) [28] [30] as well as the Realizable Two-Layer K-Epsilon model. SST k-omega utilizes a transformed version of the epsilon turbulence equation by including a cross-diffusion term [28]. The additional diffusion term allows the k-epsilon method to accurately predict the far-field solutions while simultaneously solving the near-wall problem with the more accurate k-omega model [28] [30]. The k-omega model is thought to be advantageous for adverse pressure gradients within the boundary layer and is thought to better predict wall shear stresses as will be needed to simulate the shear stress across the 3D dolphin body at high Reynolds numbers ($Re > 10^5$) [28] [31].

As opposed to the Standard Two-Layer K-Epsilon model, STAR-CCM+ recommends the Realizable Two-Layer K-Epsilon model for its overall effectiveness for both coarse mesh and fine mesh where the viscous sublayer must be resolved. Since both a fine mesh near the dolphin body surface, and a coarse mesh aft of the tail fluke is used, this realizable model helps improve accuracy in all areas of the mesh while optimizing the simulations to run on a non-HCP desktop.

5.5 Gamma Transition

To predict turbulence, a simplified model of the Gamma Re_θ method is used, termed Gamma transition [28]. As opposed to the two-equation method Gamma Re_θ which considers the momentum thickness Reynolds number (Re_θ) at transition, Gamma transition uses a singular equation only for turbulence intermittency (γ) [28] [31]. Turbulence intermittency is a local measurement of the time percentage of fluctuations within a flow, where fully laminar boundary layers exist when turbulent fluctuations exist 0% of the time ($\gamma = 0$), fully turbulent flow occurs when fluctuations are always present ($\gamma = 1$), and transition regions occur between $0 < \gamma < 1$ [31].

Developed by Menter et al. (2015), this model is suggested to be advantageous over its predecessor Gamma Re_θ, which lacks complete Galilean invariance [32]. Without identical laws of motion for all inertial scenes, Gamma Re_θ transition is not ideal for CFD simulations that include walls moving in relation to the global coordinate system [32]. By approximating the turbulence locally, calculation of momentum thickness is not necessary in Gamma Transition, and the model remains Galilean invariant [32]. In future works, this CFD model can include real-time kinematics of the up/downstrokes, where Gamma Transition may be superior to Gamma Re_θ

CHAPTER VI

EXPERIMENTAL RESULTS

6.1 Swimming Trials

Chapter 6 starts with the analysis of the swimming tensegrity dolphin before discussion of the CFD simulations and calculation of thrust and power.

6.1.1 Preliminary Tests of Simple and Complex Tail

At the early design stage of the robotic dolphin, preliminary swimming trials were done for the simple and complex tail structures. The tail beat frequency was recorded at 1.2 and 1.3 beats per second for the simple and complex designs, respectively. The corresponding velocities are given in table 6.1.

Table 6.1. Preliminary swim speeds for the simple and complex.

	Complex Design (n = 5)	**Simple Design (n = 3)**
Swim Speed	0.16 BL/s	0.24 BL/s

From table 6.1, it is suggested that at about the same frequency, the simple tail structure can reach a velocity roughly 150% higher than the complex tail structure. These measured frequencies are well within the range of the frequencies recorded for swimming dolphins throughout literature, but do not correspond with the expected swim speeds achievable by that of a real dolphin [22] [24]. Common dolphins in the wild have been measured swimming anywhere from 0.4-4 BL/s depending on whether the dolphin is steady swimming or preparing to leap out of the water [17] [21] [22] [24].

At the tail beat frequency of ~1.25 beats per second as experimentally observed, the robot is expected to travel at a speed close to 0.8BL/s, roughly 3 times faster than experimental results [22]. One reason for this low propulsion efficiency could be a lack of ample space for the dolphin to accelerate and reach a constant top speed. Another reason may be that the motor is simply not capable of providing the thrust to overcome the dolphin's friction and pressure resistance. As designed, the internal vertical plates that make up the midbody and head cage, which is fully submerged and filled with water, can be modified to have elliptical cross-sections, as opposed to flat plates that increase drag.

Not only was it found that the complex tail structure was incapable of reaching speeds as high as the simple tail structure, but also incapable of reaching high tail beat frequencies without drastically reducing the amplitude of each up/downstroke. As frequency increased near 2 Hz, the complex tail structure was nearly incapable of producing forward thrust. This disadvantage of the complex tail structure seems to be a result of the small surface area provided by the thin vertical bars (vertebrae) that leads to damping and viscous effects as the skin acts like a parachute during tail beats. The skin damping in the simple design is much less because the entire bulk of the tail structure is rigid. The suggested skin damping can be visualized in figure 6.1.

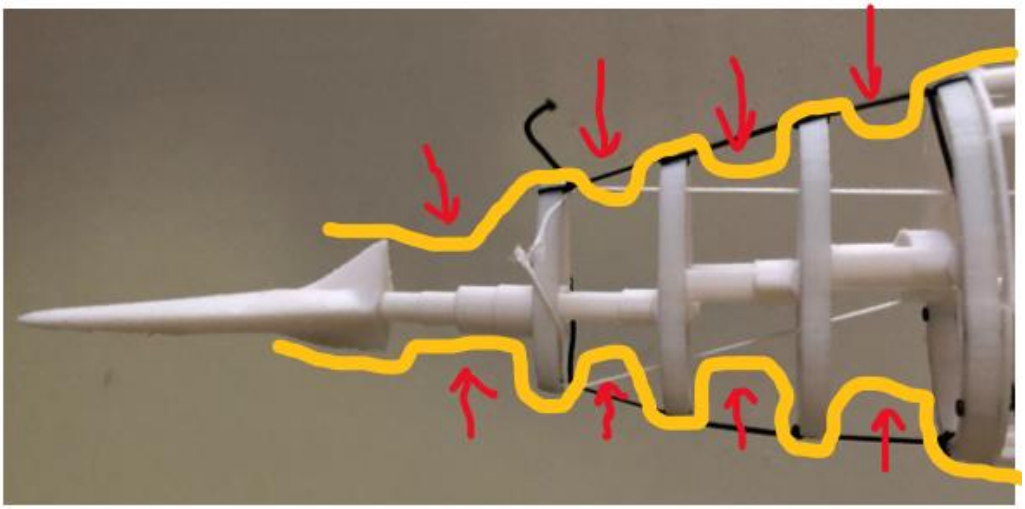

Figure 6.1. Material deformation of the neoprene skin (yellow) due to hydrodynamic forces (red arrows).

Despite the disadvantages in swimming performance, the complex design can reproduce up/downstroke kinematics with higher biomimetic accuracy because of the more precise control on each vertebral bending stiffness and angle of rotation. As discussed in Long (1997), the vertebral bending stiffness is variable along the spinal column of the dolphin, and thus for a truly biomimetic dolphin, the simple tail structure falls short. However, from the experimental results presented thus far, it is suggested that at a small scale with limited motor torque available, lower complexity structures may be desirable. In the case of low complexity tensegrity systems, the problem of tackling the nonlinear analysis of structure, control and information architecture becomes simpler with reduction in total amount of string and bar nodes. From here on out, only the simple tail structure is tested and experimentally analyzed in hopes to achieve the highest swim performance possible with limited motor torque.

6.1.2 Swimming Efficiency of Simple Tail Structure

The robotic dolphin was tested in a water tank with no wave making as seen in figure 6.2. The swimming was recorded with a mobile device and analyzed in VLC media player to analyze swim speed, tail beat frequency and amplitude, and stability of the robot.

Figure 6.2. Snapshots of the dolphin accelerating from zero forward speed.

Figure 6.3 contains the swim velocities (in body lengths per second) achieved within the wave tank over a range of tail beat frequencies between 0.8-2.4 Hz.

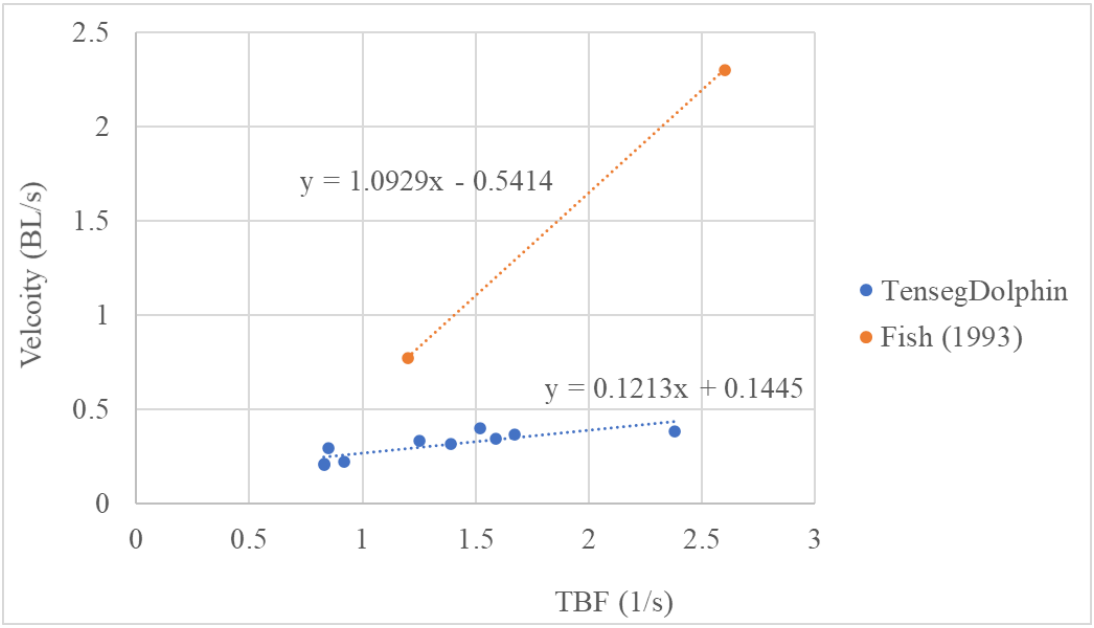

Figure 6.3. Velocity versus tail beat frequency (TBF) for the robotic and real dolphin [22].

A positive, linear trend between velocity and frequency is seen for both a real dolphin and the presented robotic dolphin and has been noted for various marine mammals that utilize hydrofoil cross-sections and thunniform gaits as a means of producing thrust [22] [33]. However, the robotic dolphin is not capable of reaching as high speeds at the same given frequencies of a real dolphin. The slope of the linear fitted curve is 9x higher for the real dolphin. Because the servo motor can no longer produce the same torque at high frequencies, the amplitude of each up/downstroke generally reduces, and swim performance falls short of biomimetic expectations. In fact, the linear trend found experimentally is only descriptive of the data when TBF is less than 1.5-2 Hz, where after this velocity seems to level out, and will eventually become zero once the TBF is so high that the motor cannot provide any torque. Figure 6.4 shows this trend in amplitude of each upstroke as a function of tail beat frequency.

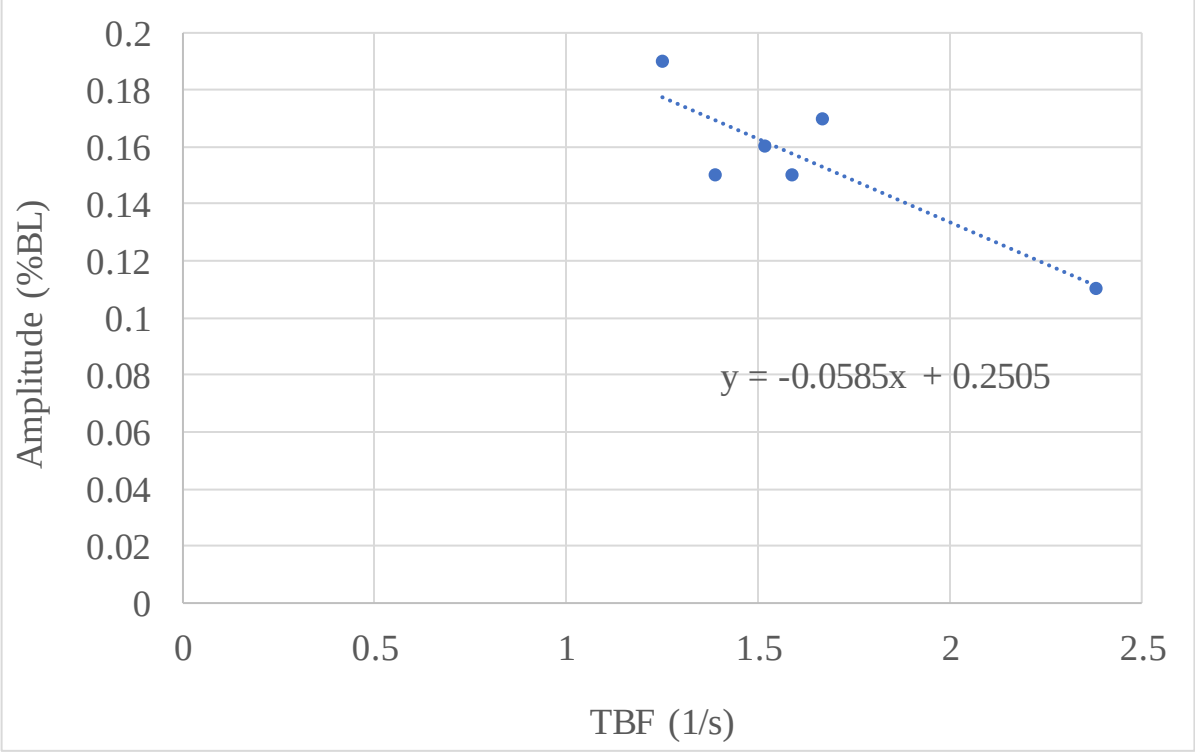

Figure 6.4. Linear, negative relationship between amplitude and TBF.

The robotic dolphin's stability was found to be impaired because of disparity between up and down undulations, where downstrokes were found to be slightly larger in amplitude. This disparity causes the dolphin to pitch upwards and surface as it swims forward and was found to be more drastic at high tail beat frequencies (TBF). The pitching dolphin at high TBF swim gaits is given in figure 6.5.

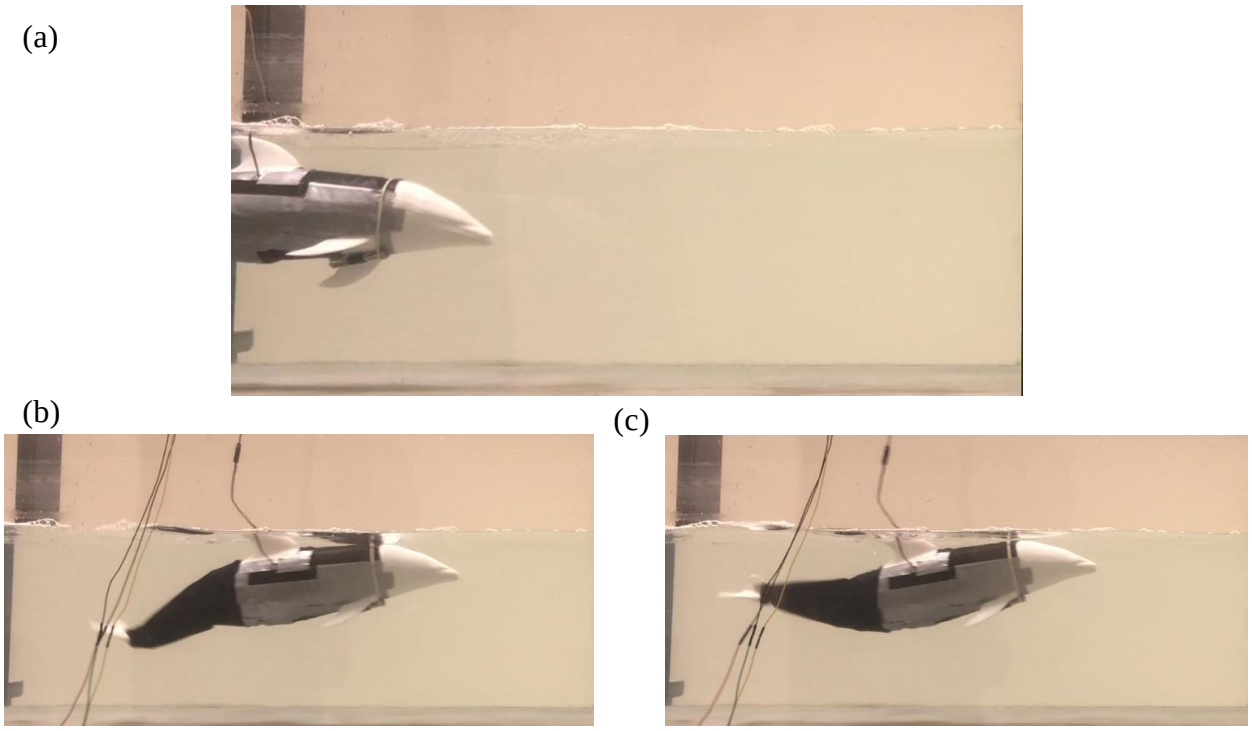

Figure 6.5. (a) The dolphin starts at neutral buoyancy, fully submerged and swims with TBF of 2.38 Hz. (b,c) Surfacing of dolphin.

Also of importance, is the time varying angle of attack of the tail fluke, which is given in figure 6.6.

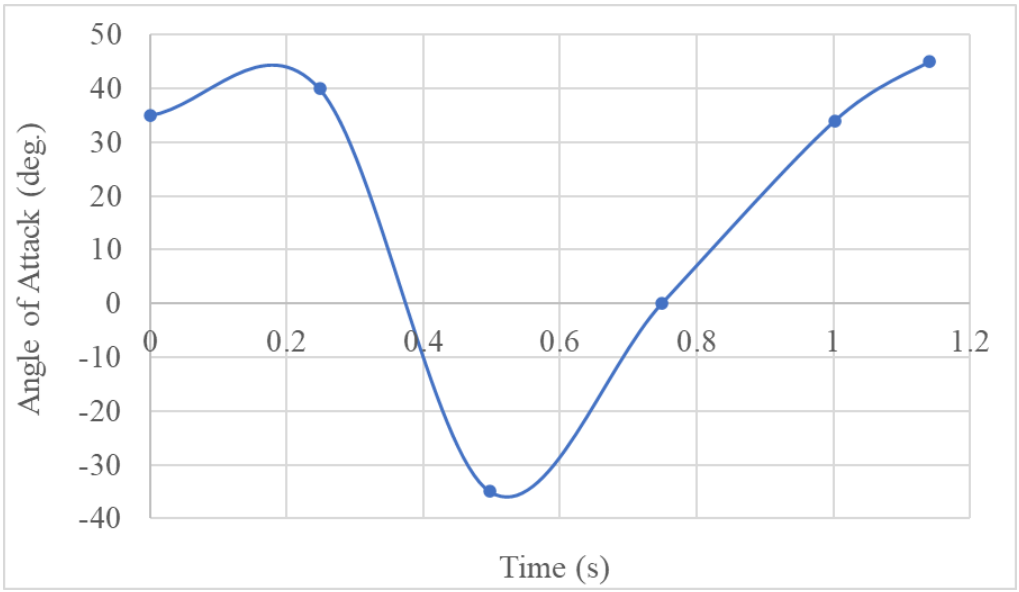

Figure 6.6. Angle of attack of the tail fluke with forward swim direction as a function of time at U = 0.4 BL/s, TBF = 1.52 Hz.

As expected, the tail fluke oscillates in a nearly sinusoidal fashion, oscillating between angles of roughly $\pm 40^{o}$, close to data from [22]. In figure 6.6, the dolphin is traveling forward at roughly 0.33 BL/s with a TBF of 1.25 Hz. It is suggested that modeling the tail fluke with a simple, low bending stiffness joint in the pre-fluke section is effective in bio-mimicking the fluke kinematics of a real dolphin as seen in Fish (1993) [22]. Without the need of a motor located at this tail fluke joint to obtain the desired angle of attack during swimming, and hence relying only on the hydrodynamic forces generated due to each up/downstroke, the robot is efficiently designed with simpler control, less electronic/power requirement, and overall, less mass.

6.2 Computational Fluid Dynamics

To visualize flow across the streamlined dolphin body, as well as to calculate coefficients of drag, the 30% scaled, straight body is simulated over a range of Reynolds numbers as in Tanaka (2019) to confirm accuracy of the CFD mesh and physics. At Re = 2e7, the frictional

drag coefficients found from the k-epsilon and k-omega turbulence models are 0.0031, and 0.0032, respectively. These drag coefficients are close in value to the result of 0.0028 found in Tanaka et al. (2019) for a k-epsilon model. The error in calculating drag coefficient may be caused mostly because the presented dolphin CAD model is decimated to 50%, as noted earlier. However, from this comparison, it is suggested that the scaled down and decimated surface of the simulated model, gives reasonable predictions of body-water interactions for simulations of dolphin bodies without the need for high computing performance (HCP).

6.2.1 k-omega and k-epsilon turbulence models

Figure 6.7 contains the wall shear stresses from both the k-epsilon and k-omega models.

(a)

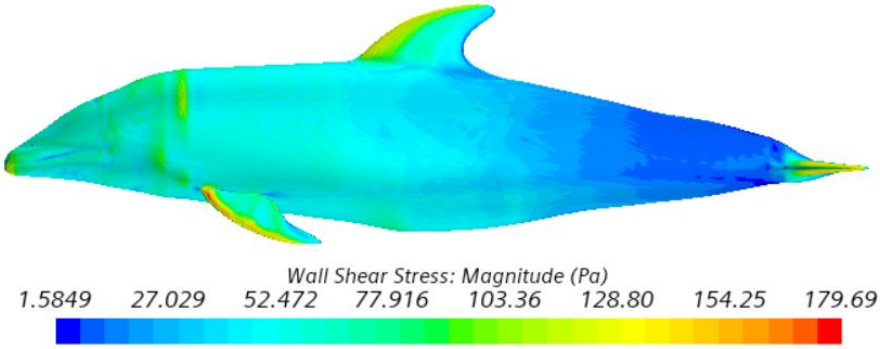

(b)

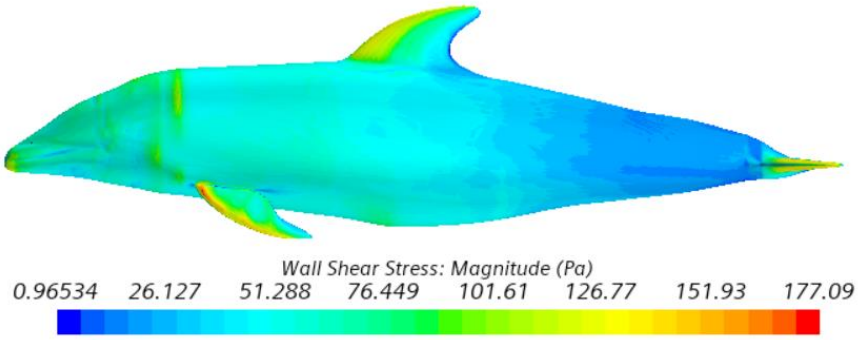

Figure 6.7. Wall shear stresses at Re = 3.1e5 (a) k-epsilon and (b) k-omega models.

By comparing (a) and (b) in figure 6.7, it can be noticed that the k-omega turbulence model predicts wall shear stresses as a consistent, decreasing gradient from nose to tail. The shear stresses in the k-epsilon model contain streaks and blotches, specifically within the trailing third of the body where boundary layer separation is expected to occur, that are not expected. These results further suggest the advatanage of k-omega SST models in predicting wall shear stresses, as summarized in table 6.2.

Table 6.2. Frictional coefficients calculated from k-epsilon and k-omega SST turbulence models at Re = 3.1e6 and Re = 2e7.

Turbulence Model	**Reynolds Number**	**C_f**
k-epsilon	3e6	0.0041
	2e7	0.0031
k-omega	3e6	0.0044
	2e7	0.0032

Table 6.2 suggests that the k-epsilon model underestimates coefficient of friction relative to k-omega, but that at high Reynolds' numbers, the two models tend to agree more. As noted earlier, the k-omega SST model is suggested to accurately predict boundary layer characteristics and wall shear stresses when adverse pressure gradients are present. These adverse pressure gradients are much less prominent at high Reynolds numbers where flow separation is expected to be delayed, and thus, the k-omega and k-epsilon models agree to a higher extent.

6.2.2 Boundary Layer and Turbulent Transition

The boundary layer mesh consists of three stacked prism layers with a total thickness of 1mm as seen in figure 6.8.

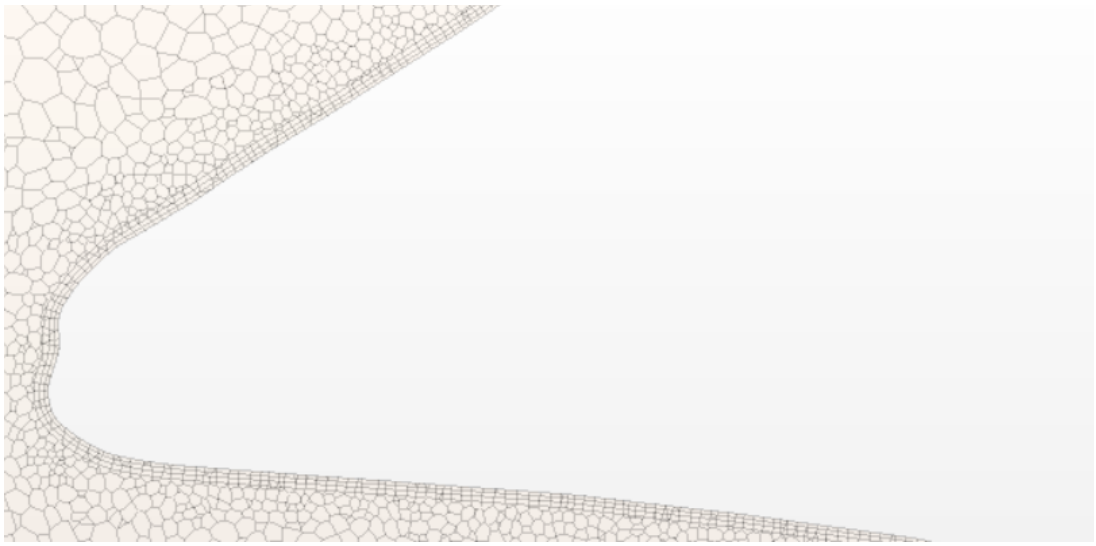

Figure 6.8. Boundary layer prism mesh as seen at rostrum.

The flow around the dolphin body has been found to transition from laminar to turbulent flow at Re > 6e5, marked by a large deviation between friction coefficients as calculated in separate laminar and turbulent models. A similar procedure of predicting turbulent transition was done by Gray (1936) [34]. When the laminar coefficient becomes roughly 90% that of the turbulent coefficient, Gray suggests the flow can no longer be analyzed as laminar. In the present analysis, only skin friction is considered, which is expected to be more than 70% of the total drag at Reynolds numbers less than 1e6 [17]. Gray's data and the data found via CFD for the present dolphin model can be observed in tables 6.3 and 6.4.

Table 6.3. Gray's estimation for turbulent transition from 1936 [34].

Reynolds Number	Drag Coefficient	
	Laminar (x 10^{-3})	Turbulent (x 10^{-3})
10^5	2.1	--
2 x 10^5	1.5	--
3 x 10^5	1.2	--
4 x 10^5	1.0	--
4 x 10^5	0.9	1.0
10^6	0.7	1.5
2 x 10^6	0.5	1.6
4 x 10^6	0.3	1.56
8 x 10^6	0.2	1.4
10^7	0.2	1.3
2 x 10^7	0.15	1.25

Table 6.4 Prediction of transition using novel CFD simulations of a straight body dolphin.

Reynolds' No.	Frictional Drag Coefficient		Laminar to Turbulent Ratio
	Laminar Flow	Turbulent Flow	
5e5	4.7 x 10^{-3}	4.9 x 10^{-3}	0.96
6e5	4.1 x 10^{-3}	4.4 x 10^{-3}	0.93
7e5	3.7 x 10^{-3}	4.6 x 10^{-3}	0.80

At Reynolds' numbers above 6e5, the turbulent kinetic energy within the wake and aft of the dorsal fin becomes significantly higher, and a turbulent sublayer forms at the body surface where shear stresses lead to fluctuations in the fluid velocities as in figure 6.9.

(a)

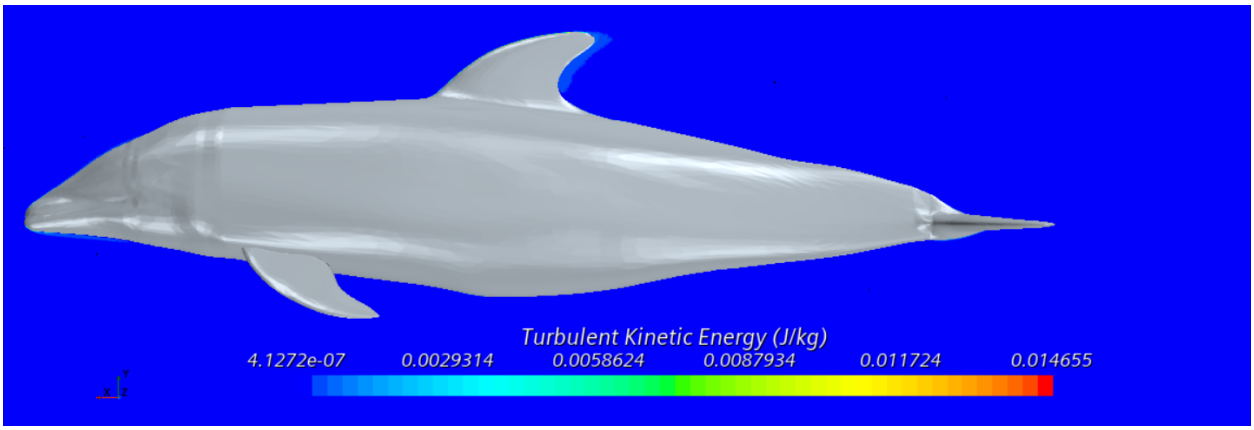

(b)

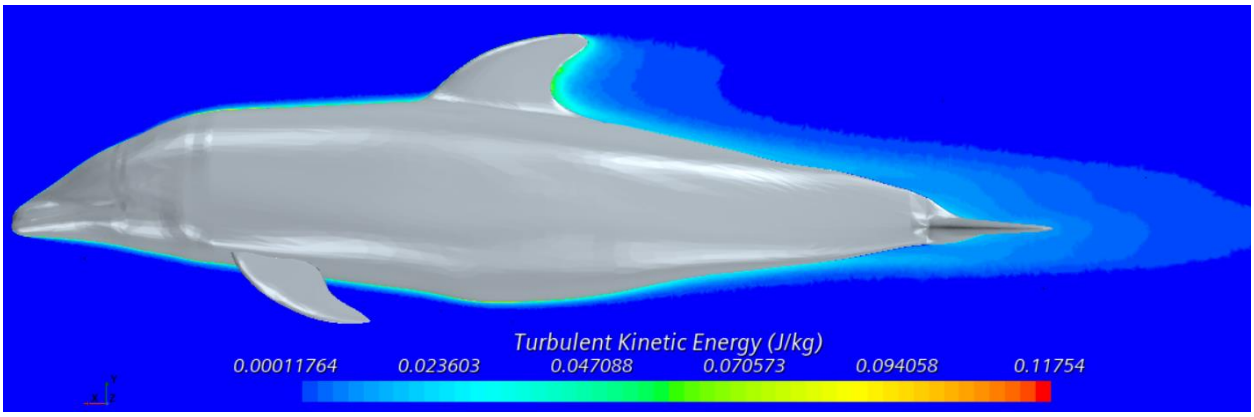

Figure 6.9. Turbulent kinetic energy for (a) Re = 5e5 and (b) 1.5e6

6.2.3 Boundary Layer Separation

To understand the separation of the boundary around the streamline dolphin, the pressure, velocity, turbulent kinetic energy, and wall shear stresses should be analyzed. It is well known that increase in turbulence will delay the onset of separation, and thus these variables should be

compared across a range of Reynolds numbers. In figure 6.10, the boundary layer thickness, calculated by assuming the boundary layer has a velocity of 99% that of the free stream velocity, is plotted along the body of the dolphin.

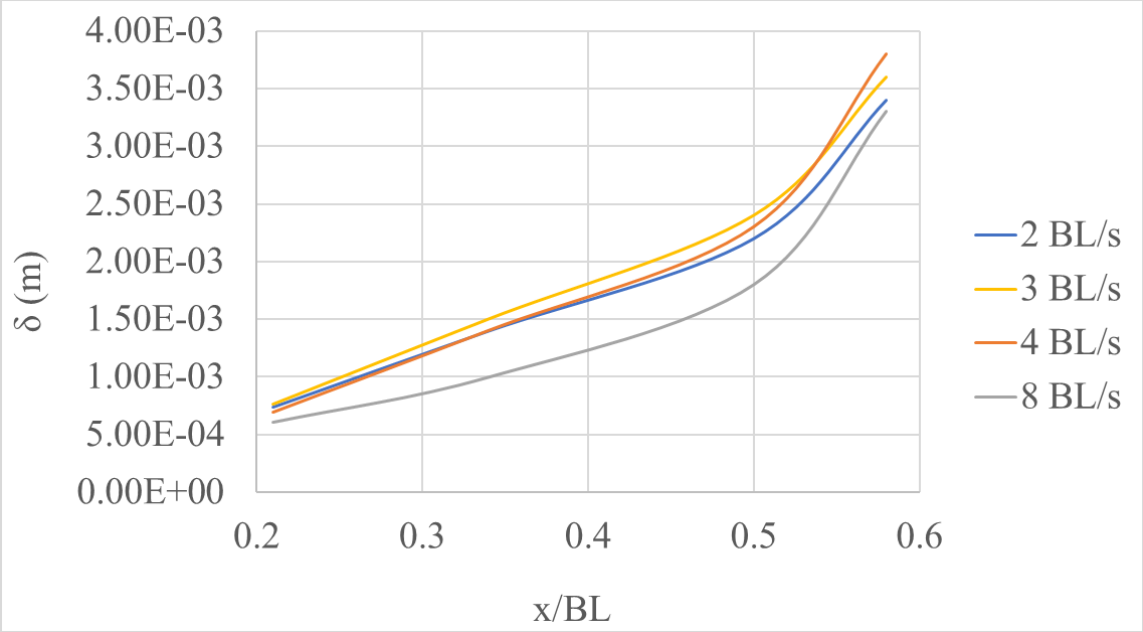

Figure 6.10. Boundary layer thickness along the length of the caudal section.

It is expected that as Reynolds number increases, the boundary layer will become thinner, and separation will be delayed. However, figure 6.10 shows that between 2-3 BL/s, boundary layer increases with increasing Reynolds number. However, above 3 BL/s, the expected thinning of the boundary layer is found to hold true. The unexpected result between 2-3 BL/s may be because the flow is near laminar conditions (Re = 7.7e5), where an increase in Reynolds' number gives rise to premature separation and high drag [35].

To approximate boundary layer separation, the wall shear stresses found within the CFD simulations for the rigid dolphin body will be analyzed as seen in figure 6.11.

(a)

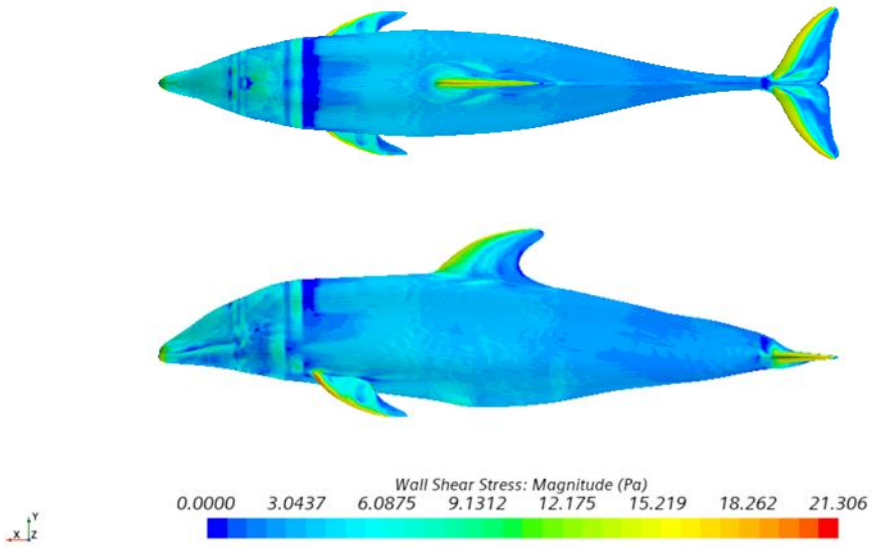

(b)

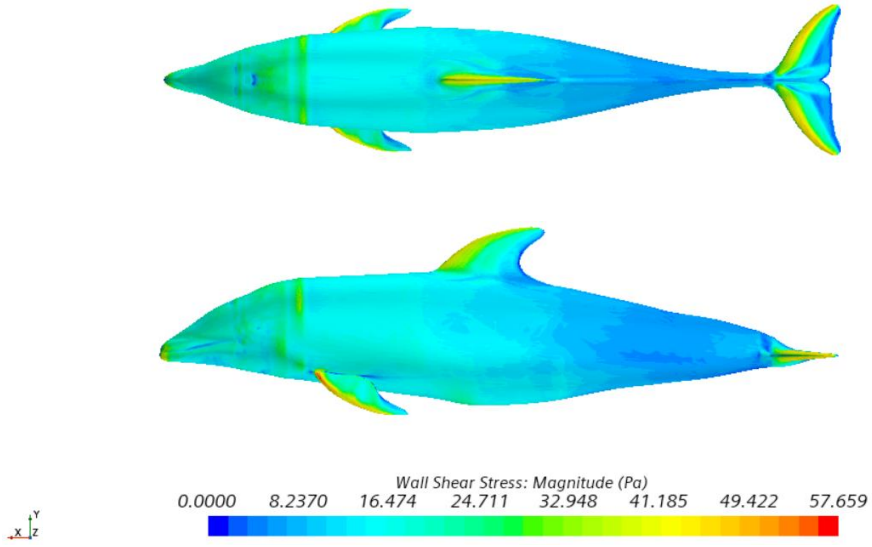

Figure 6.11. Wall shear stresses at Re = (a) 7.7e5 and (b) 1.5e6

From the figure 6.11, it can be noted that flow separation is delayed along the body length with increasing Reynolds numbers as increasing shear stresses prevent flow from

reversing its direction. At Re = 7.7e5, there is a large region of zero shear stress (denoted by dark blue) seen most notably on the top side of the caudal peduncle, in the high aspect fluke tail, and just aft of the melon. As Reynolds number increases to above 3e6, the flow stays within the boundary of the dolphin body, as denoted by increased shear stress. There are also significant areas of flow separation at low Reynolds numbers aft of the dorsal fin and at the trailing edge of the pectoral fins.

Flow separation off the trailing edge of the dorsal fin can be visualized in figure 6.12 below.

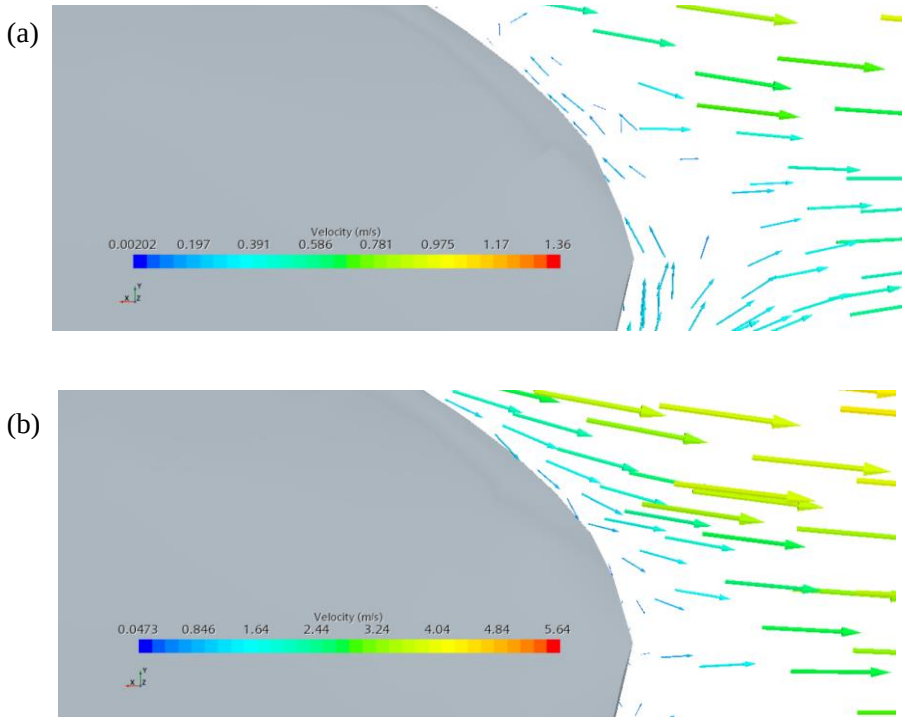

Figure 6.12. Flow over dorsal fin tip for Reynolds numbers of (a) 7.7e5 and (b) 3.1e6.

With increasing Reynolds number, the boundary layer stays attached to the dorsal fin, extending more aft and downwards along the fin. At Re = 7.7e5, flow separation occurs further up on the fin, while at Re = 3.1e6, flow separation occurs once the fin curvature begins tapering

back towards the swimming direction. The above flow visualization is in agreeance with figure 6.11, where, as Reynolds number is increased, there is significantly less areas of zero wall shear stress (areas of flow separation) along the trailing edge of the dorsal fin

Flow separation around the pectoral fins generates tip vortices like those at the wingtips of an airplane as in figure 6.13. These flow characterizations have been noted throughout literature, however, these less-novel methods used for visualizing the flow around swimming bodies have relied on techniques such as bioluminescent organisms, dyes, or air bubbles, that introduce additional errors [36] [37]. CFD techniques are advantages in the visualization of tip vortices and may predict flow properties such as boundary layer behavior and flow separation with more accuracy.

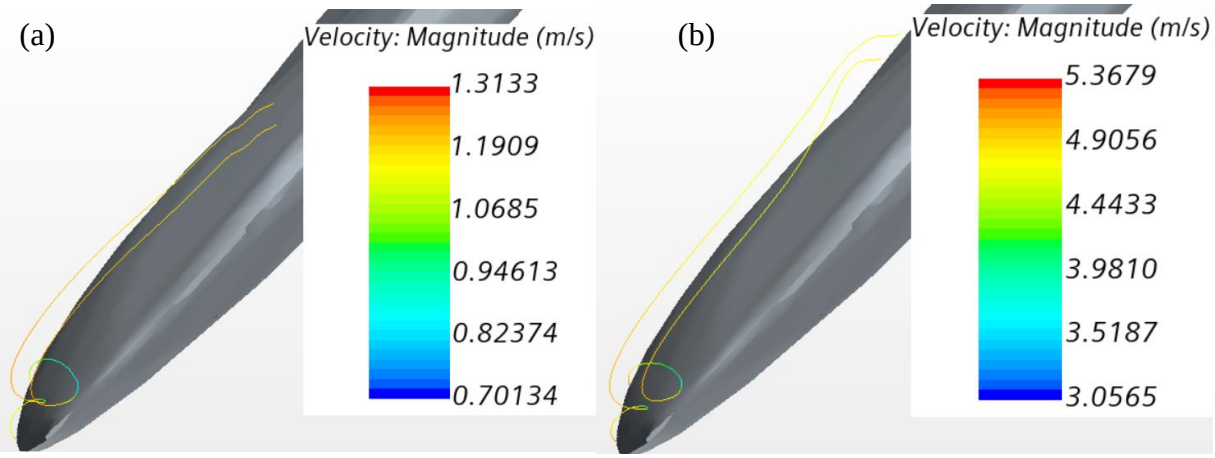

Figure 6.13. Pectoral tip vortices at (a) Re = 7.7e5 and (b) 3.1e6.

At higher Re, the vortex first sheds off the fin with a smaller diameter, which then causes a much larger second diameter, and thus these tip vortices effect the flow past the flukes and in the wake to a higher degree.

In addition to the above trends in Reynolds number, it has also been noted throughout literature that as Reynolds number increases, the wake behind the dolphin body is expected to narrow. This trend can be seen in the figure 6.14.

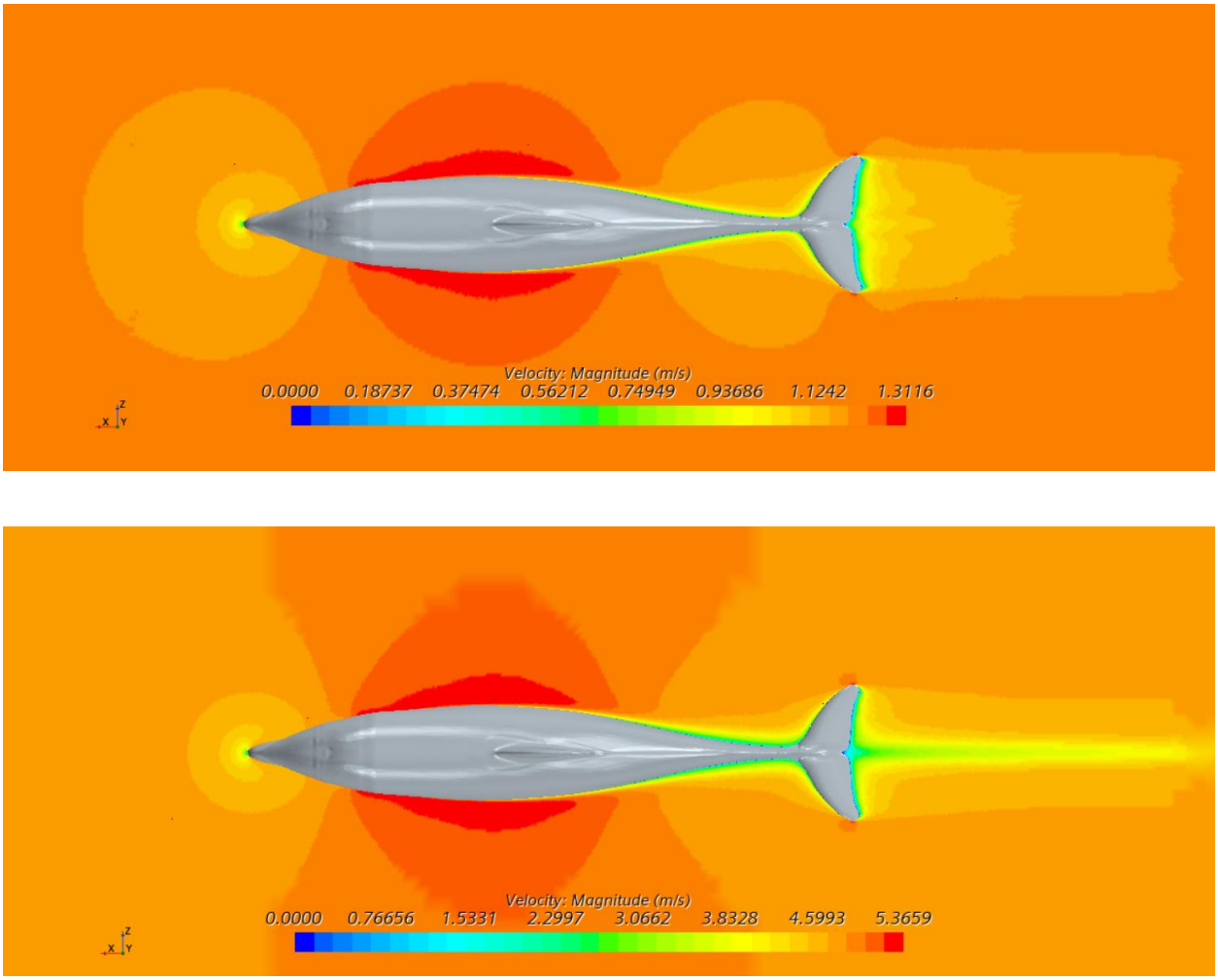

Figure 6.14. Wake visualization at Re = 7.7e5 (top) and Re = 3.1e6 (bottom).

From figure 6.14, we can see that with increasing Reynolds number, the wake behind the dolphin becomes narrower. It is also found that the pressure drag increases (by 1.2x) when Reynolds number reduces (by 0.25x) as in figure 6.14. The onset of a narrow wake and reduced pressure drag because of delayed separation is expected for turbulent flow conditions, whereas

laminar conditions give rise to premature separation and high drag [35]. This trend of pressure drag with Reynolds number was also found in Tanaka et al. (2019) [17].

6.2.4 Coefficients of Drag

Since frictional drag is dominant for the dolphin's streamlined body, as has been shown in Tanaka et al. (2019), the pressure drag, as of now, has been ignored. However, to understand the true nature of drag, the total drag coefficients found via CFD are compared to both Tanaka et al. (2019) and the ITTC-1957 method for ship resistance, as given in figure 6.15.

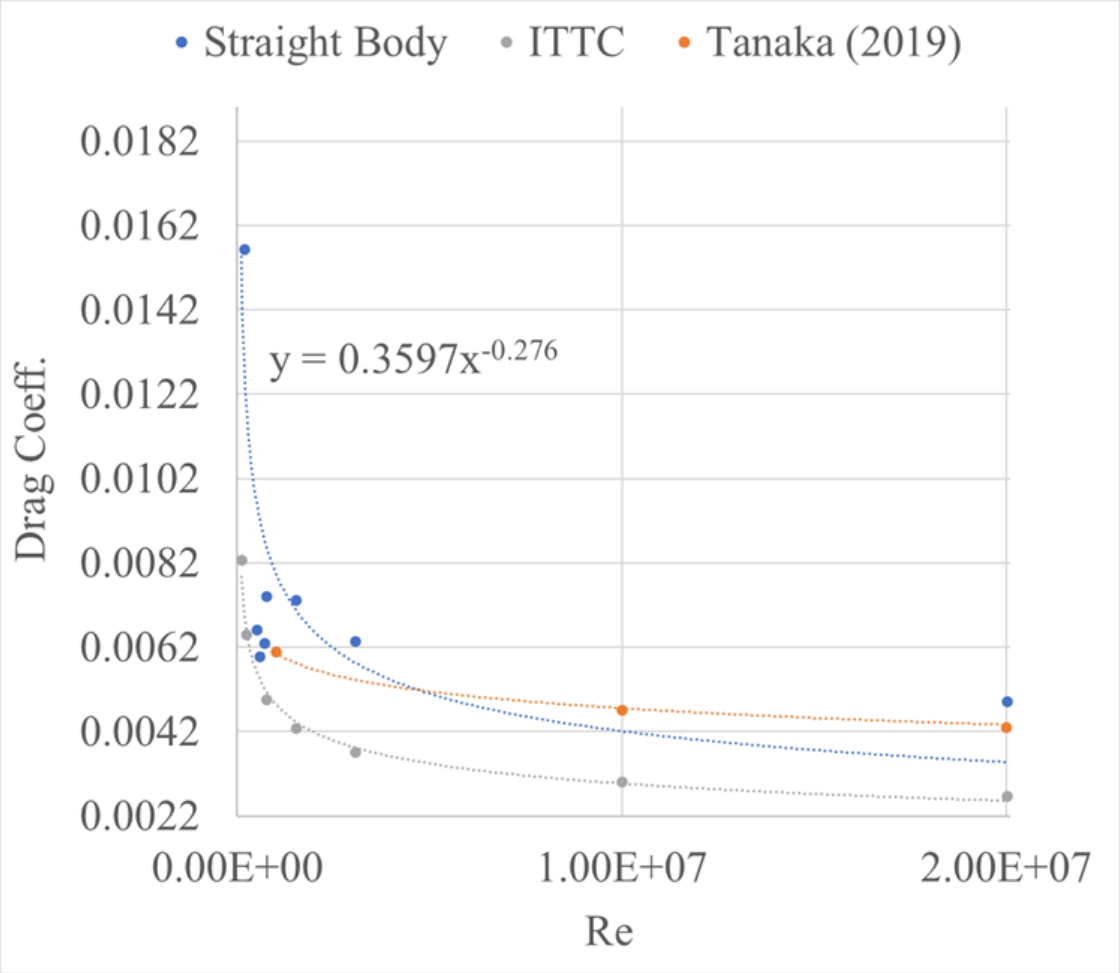

Figure 6.15. Drag coefficient as a function of Reynolds number (Re).

From figure 6.15, we see that the total drag found agrees well to the results from Tanaka et al. (2019). There is some expected error as a result of the decimated CAD model used in the presented simulations. By comparing the ITTC-1957 and the CFD results, one can calculate a form factor, which is more commonly defined as the deviation between ITTC-1957 and IITC-1978 and is most notably used for naval architecture of ships. In comparison with the CFD results, the form factors $(1 + k) = C_f^{CFD} / C_f^{ITTC57}$ are given in figure 6.16.

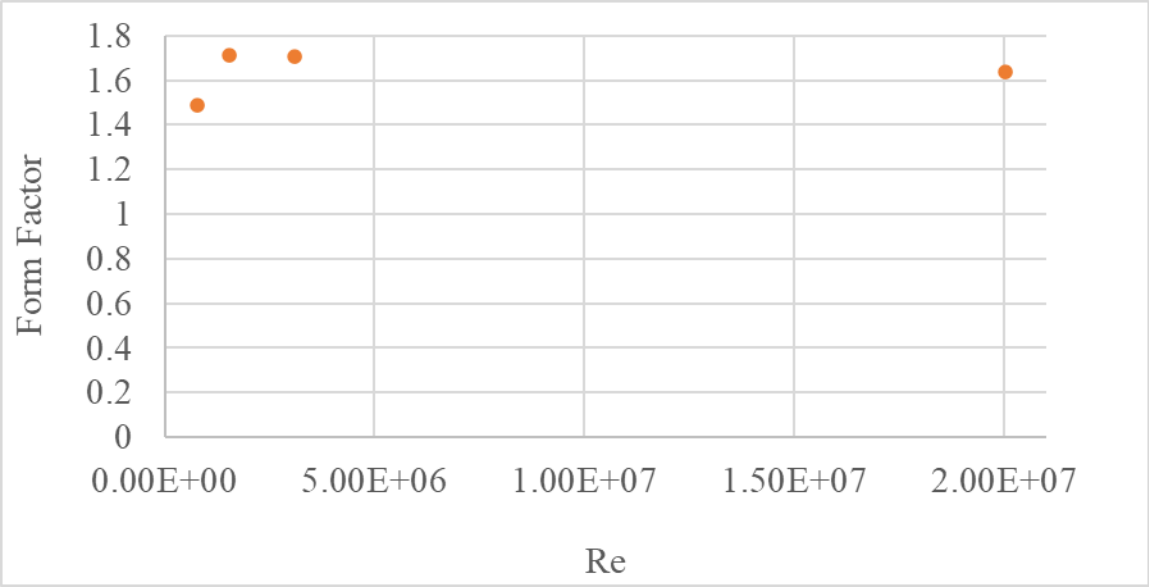

Figure 6.16. Form factor of CFD simulations in comparison to ITTC-1957.

By ignoring pressure drag, the ITTC-1957 method underpredicts the total resistance of the dolphin body with a form factor of approximately $1 + k$ = 1.5 – 1.7.

It is important to note that the drag of the rigid dolphin body is quite different from the actively swimming dolphin. Borazjani & Sotiropoulos (2008) have conducted a numerical study on carangiform fish bodies, offering insight into the prediction of drag force for undulating fish bodies in comparison to rigid bodies [38]. It was found that for undulating bodies, total drag force increases above the rigid body drag, until decreasing around Strouhal numbers of St = 0.1,

and then reaching values below the rigid body case at St = 0.25 [38]. Above St = 0.25, drag force increases for low Reynolds number (Re = 300), but decreases to 75% that of the rigid body near St = 0.6 for high Reynolds number (Re = 4000) [38]. Frictional drag, which is dominate in the case of streamlined bodies, was found to increase due to undulatory motion for all Reynolds numbers [38]. Thus, it can be concluded that the presented investigation of the rigid body dolphin may underpredict the drag, and thus future studies must be conducted to fully understand the hydrodynamics of the robotic dolphin.

6.2.5 Effects of a Bulbous Bow on Hydrodynamic Performance

Large tankers and container ships are often retrofitted with bulbous bows to increase vessel efficiencies. The bulbous bow in this case acts to reduces the bow pressure wave, and thus reduces wave-making resistance [39]. For a deeply submerged vessel, however, there are no longer surface effects. Nevertheless, bluff-nose bodies are utilized in the design of submarines, and in nature we see whales, specifically orcas, with large melons, that although are mainly used for echolocation and communication, may offer some sort of increased hydrodynamic performance. To investigate the potential effects of a bulbous bow, or in this case a bulbous melon, in comparison to a more streamline dolphin body, the dolphin model acquired from Tanaka et al. (2019) is further edited using Blender to generate an inflated melon, as can be seen in figure 6.17.

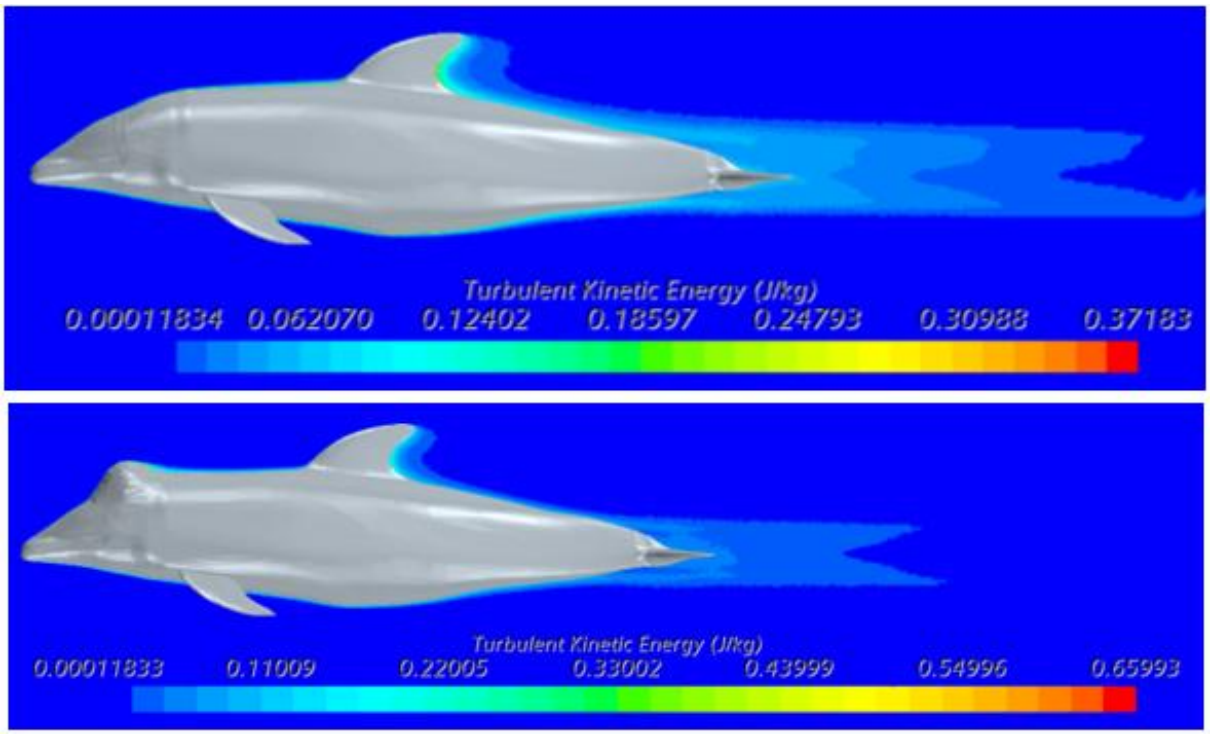

Figure 6.17. Wake effects of a dolphin body with a (a) streamlined melon and (b) bulbous melon at Re = 3.1e6.

The data in figure 6.17 suggests that a bulbous melon will narrow the wake and delay separation of the boundary layer, at typical speeds of swimming dolphins. With increased surface area, frictional drag is expected to increase, however surface-averaged wall shear stresses changed by an insignificant percent difference (0.4%) for the bulbous melon. Note that despite the delay of flow separation, the magnitude of turbulence increases in case of the bulbous melon. There is expected to be additional computational error as a result of the facets in the inflated melon, which are characteristic of sharp edges as opposed to the desired smooth, continuous surface of a real dolphin melon.

6.3 Calculation of Thrust

Following the procedure outlined in Tanaka et al. (2019) the thrust (T) and power (P) are calculated as

$$T = m\vec{a} \cdot \frac{\vec{v}}{|\vec{v}|} + (m - \rho V)\vec{g}\frac{\vec{v}}{|\vec{v}|} - \frac{1}{2}\rho|\vec{v}|^2 S_{surface} C_D(|\vec{v}|) - M_{added}\vec{a}\frac{\vec{v}}{|\vec{v}|} \quad (42)$$

and

$$P = T|\vec{v}| \quad (43)$$

where m is mass of the robot, $\vec{a}$ is acceleration, $\vec{v}$ is velocity, ρ is density of water, V is the volume of robot, $S_{surface}$ is the surface area of the robot, $C_D(|\vec{v}|)$ is the drag coefficient as a function of the magnitude of swim velocity found via CFD, and M_{added} is the added mass of the robot [17]. For added mass, the robot is assumed to be a prolate spheroid and thus M_{added} is given by

$$M_{added} = \frac{4\pi}{3}\kappa\rho r_a^2 r_b^2,\ \kappa = \frac{\alpha}{2-\alpha},\ \alpha = \frac{1-e^2}{e^3}\left(ln\frac{1+e}{1-e} - 2e\right),\ e = \sqrt{\frac{r_a^2 - r_b^2}{r_a^2}} \quad (44)$$

as presented by Brennen (1982) [17] [41]. The variables in equations 60 and 61 are summarized in table 6.5 below.

Table 6.5. Robot mass properties and geometric dimensions. $C_D(|\vec{v}|)$ is found from via CFD.

m (submerged	$S_{surface}$	**V**	r_a	r_b	e	κ	M_{added}
2 kg	0.13 m^2	0.002 m^3	0.28 m	0.045 m	0.99	0.36	0.002 kg

Using manual digitization, the center of mass of the dolphin was tracked at time-steps of roughly 0.1s. From this digitalization method, the instantaneous values of thrust and power in the direction of motion (i.e., forward swim direction, and change in depth) were calculated, as given in figure 6.18 and figure 6.19.

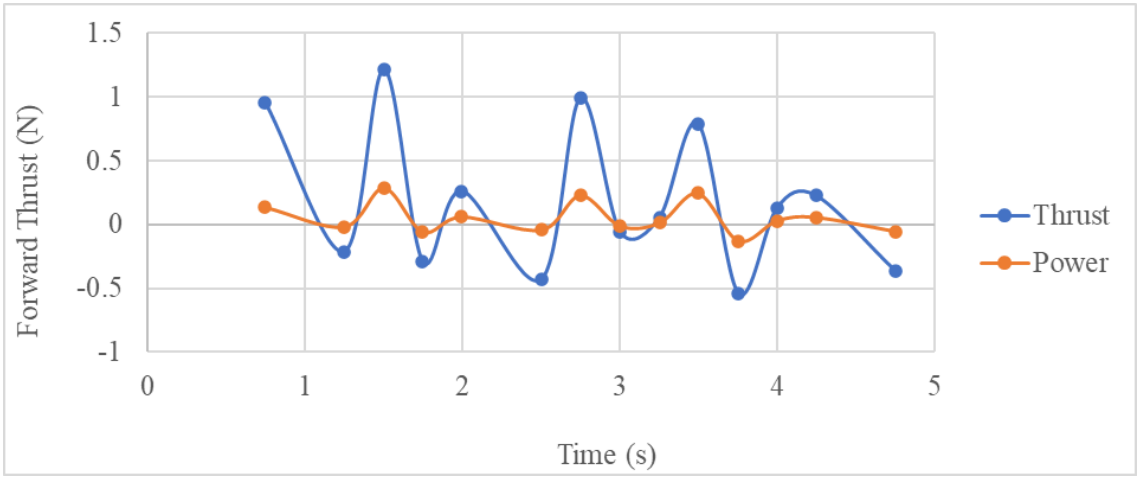

Figure 6.18. Thrust and power in forward direction at tail beat frequency of 1.67Hz.

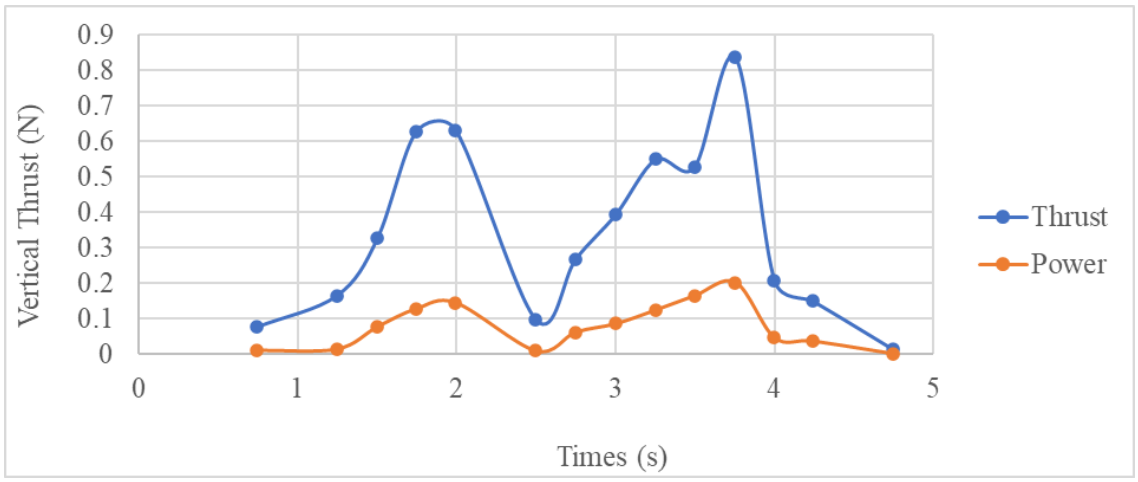

Figure 6.19. Thrust and power in vertical direction at tail beat frequency of 1.67Hz.

From figure 6.18 it is seen that forward thrust is on average positive (+0.21 N) despite the presence of several negative values, meaning that the dolphin travels forward, but with some

degree of efficiency loss. By definition of a force equaling the acceleration of a mass, this thrust would accelerate the dolphin mass by 0.1 m/s^2. By monitoring the change of velocity of the dolphin starting from rest, the acceleration was estimated at 0.07 m/s^2, agreeing close to the calculated thrust. Error is expected since the frame rate of the mobile camera is low, and because the center of mass is estimated by manual digitalization and is thus not consistent for each time step.

From figure 6.19, thrust and power in the vertical direction is found to always be positive, correlating to the previously noted tendency for the robot to surface as it swims forward.

CHAPTER VII

CONCLUSIONS AND FUTURE WORK

In conclusion, this thesis offers an overview of tensegrity theory as applied to the design of the first known robotic tensegrity dolphin. The robot was 3D printed (PLA) at 30% scale of a real dolphin. It was found that at this scale and being powered by a low torque (35kg-cm) motor, a simple tensegrity structure (i.e., one with less vertebrae) is more efficient in producing forward thrust. The range of Strouhal numbers (St = fA/U, where f is TBF, A is tail beat amplitude, and U is forward swim speed) was found to be $0.57 < St < 0.84$. Most swimming and flying animals have evolved to achieve gaits within the region of $0.25 < St < 0.35$, to amplify the efficiency of foil oscillations [8].

The relationship between swim speed and tail beat frequency of the robot was found to be linear, as expected for real dolphins, however, tail beat amplitude was severely reduced at frequencies above 1.5 Hz due to the low torque motor.

To progress the previously written codes for the analysis of 2D morphing airfoils at low angles of attack, this study has applied said codes to model the high amplitude undulation of both a 2D and 3D dolphin caudal region. Alongside these dynamic simulations, CFD analysis of the dolphin body at various swim speeds and body geometries were conducted to calculate and visualize flow characteristics around the streamlined dolphin body.

Future studies can be conducted to progress the robotic swim performance, first by installing a high torque servomotor, which may require the scale of the robot to be increased. To help choose a proper motor, it should be noted that throughout literature, dolphins have been found to require roughly 20-90 Watts per kg of body mass to achieve proper swim performance

[17]. Secondly, performance can be increased by increasing the number of actuating strings such that each rigid vertebra is actuated to a predetermined flexion angle. Increasing the number of actuating strings will allow the implementation of information architecture not yet explored for the tensegrity dolphin.

To improve the presented CFD methods, dynamic simulations of the actively swimming dolphin body should be a major focus of future studies to understand the true flow characteristics and coefficients of drag of the swimming robot. As discussed earlier, it was found in Borazjani & Sotiropoulos (2008) that undulatory motion of carangiform bodies leads to an increase in frictional drag [38]. Similar studies have been conducted such as presented in Borazjani & Sotiropoulos (2009) for anguilliform swimmers [42], and Borazjani (2013) for fast start maneuvers [43]. These studies offer important data for actively swimming fish bodies that is crucial in overcoming the limitations of the presented CFD studies.

Lastly, this thesis focuses on the biomimetic properties of tail beat frequency, tail beat amplitude and fluke angle of attack. However, it is beneficial to describe the tail undulation as a body wave, such as the muscle wave contractions that travel down the bodies of fish and marine mammals. Thus, future studies may define a sinusoidal body wave for the flexing tail structure to reproduce the swim performance of dolphins to a higher degree, as outlined in Akbarzadeh and Borazjani (2019) [44].

REFERENCES

[1] R. B. Fuller. US patent 3.063.521 Tensile integrity structures. United States Patent Office, 1959.

[2] Skelton, Robert E., and Mauricio C. De Oliveira. Tensegrity systems. Vol. 1. New York: Springer, 2009.

[3] Chen, Muhao, Jiacheng Liu, and Robert E. Skelton. "Design and control of tensegrity morphing airfoils." Mechanics Research Communications 103 (2020): 103480.

[4] Liedl, Tim, et al. "Self-assembly of three-dimensional prestressed tensegrity structures from DNA." Nature nanotechnology 5.7 (2010): 520-524.

[5] Goyal, Raman, and Robert E. Skelton. "Tensegrity system dynamics with rigid bars and massive strings." Multibody System Dynamics 46.3 (2019): 203-228.

[6] Goyal, Raman, Manoranjan Majji, and Robert E. Skelton. "Integrating Structure, Information Architecture and Control Design for Tensegrity Systems." arXiv preprint arXiv:2011.10838 (2020).

[7] Barrett, D. S., Triantafyllou, M. S., Yue, D. K. P., Grosenbaugh, M. A., & Wolfgang, M. J. "Drag reduction in fish-like locomotion." (1999).

[8] Triantafyllou, Michael S., and David S. Barrett. "Propulsion mechanism employing flapping foils." U.S. Patent No. 5,401,196. 28 Mar. 1995.

[9] Triantafyllou, Michael S., and George S. Triantafyllou. "An efficient swimming machine." Scientific american 272.3 (1995): 64-70.

[10] Kent, W. Saville. "Fish distinguished by their action." (1873): 263-264.

[11] Gray, J. "The movement of fish with special reference to the eel." J. exp. Biol 10 (1933): 88-104.

[12] Lighthill, M. J. "Note on the swimming of slender fish." Journal of fluid Mechanics 9.2 (1960): 305-317.

[13] Lighthill, Michael James. "Large-amplitude elongated-body theory of fish locomotion." Proceedings of the Royal Society of London. Series B. Biological Sciences 179.1055 (1971): 125-138.

[14] Lighthill, Michael James. "Aquatic animal propulsion of high hydromechanical efficiency." Journal of Fluid Mechanics 44.2 (1970): 265-301.

[15] Yu, Junzhi, Zongshuai Su, Ming Wang, Min Tan, and Jianwei Zhang. "Control of yaw and pitch maneuvers of a multilink dolphin robot." IEEE Transactions on robotics 28.2 (2011): 318-329.

[16] Yu, Junzhi, Zongshuai Su, Zhengxing Wu, and Min Tan. "Development of a fast-swimming dolphin robot capable of leaping." IEEE/ASME Transactions on Mechatronics 21.5 (2016): 2307-2316.

[17] Tanaka, Hiroto, Gen Li, Yusuke Uchida, Masashi Nakamura, Teruaki Ikeda, and Hao Liu. "Measurement of time-varying kinematics of a dolphin in burst accelerating swimming." PloS one 14.1 (2019): e0210860.

[18] Chen, Bingxing, and Hongzhou Jiang. "Swimming performance of a tensegrity robotic fish." Soft robotics 6.4 (2019): 520-531.

[19] L. Wen, T. M. Wang, G. H. Wu and J. H. Liang "Hydrodynamic investigation of a self-propelled robotic fish based on a force-feedback control method." Bioinspiration & biomimetics 7.3 (2012): 036012.

[20] Fish, Frank E. "The myth and reality of Gray's paradox: implication of dolphin drag reduction for technology." Bioinspiration & biomimetics 1.2 (2006): R17.

[21] Long, John H., D. Ann Pabst, William R. Shepherd, and William A. Mclellan. "Locomotor design of dolphin vertebral columns: bending mechanics and morphology of Delphinus delphis." Journal of Experimental Biology 200.1 (1997): 65-81.

[22] Fish, Frank E. "Power output and propulsive efficiency of swimming bottlenose dolphins (Tursiops truncatus)." Journal of Experimental Biology 185.1 (1993): 179-193.

[23] Chen, Bingxing, and Hongzhou Jiang. "Swimming performance of a tensegrity robotic fish." Soft robotics 6.4 (2019): 520-531.

[24] Videler, J. O. H. N., and P. A. U. L. I. N. E. Kamermans. "Differences between upstroke and downstroke in swimming dolphins." Journal of Experimental Biology 119.1 (1985): 265-274.

[25] Pabst, D. Ann. "Intramuscular morphology and tendon geometry of the epaxial swimming muscles of dolphins." Journal of Zoology 230.1 (1993): 159-176.

[26] Guo, Shangkun, et al. "Design Of Flexible Tail Fin Propeller For Bionic Dolphin." 2020 3rd International Conference on Unmanned Systems (ICUS). IEEE, 2020.

[27] Fish, Frank E. "Balancing requirements for stability and maneuverability in cetaceans." Integrative and comparative biology 42.1 (2002): 85-93.

[28] Simcenter STAR-CCM+ User Guide. file:///C:/Program%20Files/Siemens/15.06.008/STAR-CCM+15.06.008/doc/en/online/index.html#page/STARCCMP%2FGUID-B52EEA73-AA46-4E60-9F85-4779E3C7397D.html%23

[29] Dr. David Allen. Course notes from OCEN 678: Fluid Dynamics for Ocean and Environmental Engineering. Texas A&M University. Fall 2019.

[30] Menter, Florian R. "Two-equation eddy-viscosity turbulence models for engineering applications." AIAA journal 32.8 (1994): 1598-1605.

[31] Wimshurst, Aidan (2019, July 30). "[CFD] The Transition SST (gamma - Re_theta) model." YouTube. youtube.com/watch?v=5htknS9uVEk&ab_channel=FluidMechanics101

[32] Menter, Florian R., Pavel E. Smirnov, Tao Liu, and Ravikanth Avancha. "A one-equation local correlation-based transition model." Flow, Turbulence and Combustion 95.4 (2015): 583-619.

[33] Fish, Frank E. "Comparative kinematics and hydrodynamics of odontocete cetaceans: morphological and ecological correlates with swimming performance." Journal of Experimental Biology 201.20 (1998): 2867-2877.

[34] Gray, James. "Studies in animal locomotion: VI. The propulsive powers of the dolphin." Journal of experimental biology 13.2 (1936): 192-199.

[35] Webb, Paul W., and WEBB PW. "Hydrodynamics and energetics of fish propulsion." (1975).

[36] Rohr, James, et al. "Experimental approaches towards interpreting dolphin-stimulated bioluminescence." Journal of Experimental Biology 201.9 (1998): 1447-1460.

[37] Webb, P. W. “Hydrodynamics: Nonscombroid Fish.” Fish Physiology,

Vol. VII., W. S. Hoar and D. J. Randall, eds. Academic Press, New York. (1978):

190-239

[38] Borazjani, Iman, and Fotis Sotiropoulos. "Numerical investigation of the hydrodynamics of carangiform swimming in the transitional and inertial flow regimes." Journal of experimental biology 211.10 (2008): 1541-1558.

[39] Dr. Jeffrey Falzarano. Course notes from OCEN 621: Naval Architecture. Texas A&M University. Spring 2021.

[40] Webb, Angus P., et al. "Can Lighthill's elongated body theory predict hydrodynamic forces in underwater undulatory swimming?." Procedia Engineering 34 (2012): 724-729.

[41] Brennen, C. E. "A Review of Added Mass and Fluid Inertial Forces." (1982).

[42] Borazjani, Iman, and Fotis Sotiropoulos. "Numerical investigation of the hydrodynamics of anguilliform swimming in the transitional and inertial flow regimes." Journal of Experimental Biology 212.4 (2009): 576-592.

[43] Borazjani, Iman. "The functional role of caudal and anal/dorsal fins during the C-start of a bluegill sunfish." Journal of Experimental Biology 216.9 (2013): 1658-1669.

[44] Akbarzadeh, A. M., and I. Borazjani. "Reducing flow separation of an inclined plate via travelling waves." Journal of Fluid Mechanics 880 (2019): 831-863.